

# Simultaneous inversion for crustal thickness and anisotropy by multiphase splitting analysis of receiver functions

Frederik Link<sup>1</sup>, Georg Rumpker<sup>1</sup> and Ayoub Kaviani<sup>1</sup>

*Institute for Geosciences, Department of Geosciences, Goethe-University Frankfurt, Frankfurt, DE-60438, Germany. E-mail: link@geophysik.uni-frankfurt.de*

Accepted 2020 September 7. Received 2020 August 23; in original form 2020 April 6

## SUMMARY

We present a technique to derive robust estimates for the crustal thickness and elastic properties, including anisotropy, from shear wave splitting of converted phases in receiver functions. We combine stacking procedures with a correction scheme for the splitting effect of the crustal converted Ps-phase and its first reverberation, the PpPs-phase, where we also allow for a predefined dipping Moho. The incorporation of two phases stabilizes the analysis procedure and allows to simultaneously solve for the crustal thickness, the ratio of average *P*- to *S*-wave velocities, the percentage of anisotropy and the fast-axis direction. The stacking is based on arrival times and polarizations computed using a ray-based algorithm. Synthetic tests show the robustness of the technique and its applicability to tectonic settings where dip of the Moho is significant. These tests also demonstrate that the effects of a dipping layer boundary may overprint a possible anisotropic signature. To constrain the uncertainty of our results we perform statistical tests based on a bootstrapping approach. We distinguish between different model classes by comparing the coherency of the stacked amplitudes after moveout correction. We apply the new technique to real-data examples from different tectonic regimes and show that coherency of the stacked receiver functions can be improved, when anisotropy and a dipping Moho are included in the analysis. The examples underline the advantages of statistical analyses when dealing with stacking procedures and potentially ambiguous solutions.

**Key words:** Statistical methods; Body waves; Crustal imaging; Seismic anisotropy; Crustal structure.

## INTRODUCTION

Seismic anisotropy provides important constraints on complex structures and internal processes of the earth. In the crust, anisotropy can originate from diverse tectonic scenarios. Dyke intrusions and melt filled cracks can cause anisotropic effects in volcanic regions (Blackman & Kendall 1997; Mainprice 1997; Savage 1999). Similarly, at shallow depths, significant anisotropy can be caused by alternating thin sedimentary layers, which are (usually) horizontal or may have been tilted by tectonic forces (Backus 1962; Savage 1999). An alignment of cracks in the upper crust due to a stress field (Christensen 1966; Nur & Simmons 1969; Nur 1971; Crampin 1987; Yousef & Angus 2016), can also cause anisotropy and a directional dependency of the nature of seismic wave field. Additionally, most of the crustal minerals are intrinsically anisotropic, which can cause a bulk seismic anisotropy when they are aligned due to strain. In the crust, this effect is relevant only for deeper layers, where phyllosilicates are assumed to align with a possible flow direction (Babuska & Cara 1991; Barruol & Mainprice 1993; Ji *et al.* 1993; McNamara & Owens 1993). In contrast to the multiple possible causes for anisotropy in the crust, seismic anisotropy in the mantle is believed to originate mainly from the preferred alignment of minerals (also referred to as crystallographic preferred orientation, CPO), primarily olivine, reflecting the direction of the mantle flow. Therefore, the study of seismic anisotropy has long been used to infer mantle deformation related to tectonic processes from seismic wavefield observations at the surface.

To explore the anisotropic properties in different regimes, several techniques have been developed during the last decades. When entering an anisotropic medium, seismic shear waves are split into two orthogonally polarized phases that travel with different wave-speeds leading to increasingly separated phases during propagation. The most common method to examine this effect is the analysis of shear wave splitting, mainly applied to core-phases (e.g. SKS, SKKS, PKS) as their polarization at the base of the mantle is known. *S* waves of local deep earthquakes have also been analysed using these techniques to study the mantle wedge in subduction zones (Ando *et al.* 1980; Bowman & Ando 1987; Savage *et al.* 2016; Reiss *et al.* 2018). The methods are based on a single-event analysis and aim at removal of the anisotropic effect characterized by two splitting parameters: splitting time and fast polarization direction (Bowman & Ando 1987; Silver & Chan 1988,

1991; Shih *et al.* 1989). Several toolboxes have been developed to simplify the analysis procedure and to facilitate its application to large data sets (e.g. Wüstefeld *et al.* 2008; Savage *et al.* 2010; Reiss & Rumpker 2017).

For teleseismic phases, the split waveforms are potentially affected by crustal anisotropy, as they provide only limited information on the depth origin of the anisotropic effects (e.g. Latifi *et al.* 2018). Crustal anisotropy has also been identified and isolated using tomographic techniques. Regional and local earthquakes can be used to derive  $P$ -wave anisotropy in tomographic studies (Zhao *et al.* 1992, 2016; Wang & Zhao 2008, 2013; Cheng *et al.* 2016; Hua *et al.* 2017). In regions of limited seismic activity, surface waves generated from ambient noise have also been used to infer the anisotropy of the crust and upper mantle (e.g. Fry *et al.* 2010).

While these studies show the significance of considering the crust in the analysis of anisotropy, the methods require dense event and receiver locations to account for lateral and vertical variations. Receiver function techniques are advantageous as they are sensitive to seismic discontinuities and can be applied to single seismic stations. Thus, anisotropic properties can be relatively well defined laterally, while the identification of discontinuities allows constraints on the depth range. Receiver functions for anisotropic media exhibit unique characteristics, due to the azimuthal variation of the wave speed and  $S$ -wave splitting (Rumpker *et al.* 2014). Transverse-component energy of the  $P_s$ -phase converted at the Moho is one indicator for crustal anisotropy and/or a dipping interface (Levin & Park 1997; Savage 1998). Waveform modeling has been used to identify characteristic features in receiver functions to distinguish between different models that include anisotropic properties (Levin & Park 1997; Sambridge 1999; Frederiksen & Bostock 2000; Okaya & McEvelly 2003; Eckhardt & Rabbel 2011; Schulte-Pelkum & Mahan 2014; Wirth & Long 2014). A more direct approach to derive anisotropic properties of the crust is the application of shear wave splitting analysis techniques, as a direct inference of the splitting time and symmetry axis direction is possible (Nagaya *et al.* 2008; Liu & Niu 2012; Sun *et al.* 2015; Wang *et al.* 2016). Another method that allows to analyse for anisotropy (including a plunging symmetry axis) as well as for a dipping interface is the harmonic decomposition, which also analyses the periodic variation of the polarization and arrival time of the  $P_s$ -phase (Bianchi *et al.* 2010, 2015; Bianchi & Bokelmann 2014; Cossette *et al.* 2016). However, a discrimination between a plunging symmetry axis and a dipping interface is not possible. Recently, the energy minimization of the transverse component has been combined with the analysis of periodic variation of the arrival times of the crustal  $P_s$  phase to simultaneously derive the dip of the Moho and anisotropic properties of the crust (Wang *et al.* 2020). For this approach an approximation of the isotropic 1-D-velocity structure of the crust has to be known.

Energy minimization of the transverse component in combination with periodic variation of the arrival times of the crustal  $P_s$  phase was also used to stabilize the analysis procedure (Rumpker *et al.* 2014). The technique has been applied by Kaviani & Rumpker (2015) to derive a generalization of the  $H$ - $\kappa$ -stacking algorithm of Zhu & Kanamori (2000) to anisotropic media. As shown earlier (Hammond 2014), neglecting the anisotropy in the crust, the thickness and seismic velocity ratio may be misestimated when the (isotropic) stacking procedure of Zhu & Kanamori (2000) is applied. In contrast, Kaviani & Rumpker (2015) first determine the bulk anisotropy (given by a percentage value and a fast-axis orientation) within the crust from analysis of the  $P_s$  phase. In a second step, this information is used to compute arrival times of the converted and multiple phases for the  $H$ - $\kappa$ -stacking procedure based on the code ‘raysum’ (Frederiksen & Bostock 2000).

In the method presented here we simultaneously infer the structural and anisotropic properties of the crust (assuming a single-layer model), while also allowing for a dipping Moho. The algorithm solves for the depth of the (Moho-) discontinuity, the ratio of the average  $P$ - and  $S$ -wave velocities, the strength of anisotropy, and the direction of the fast or slow symmetry axis in a single step. For most of the above-mentioned methods, a more or less complete azimuthal coverage is required to infer crustal anisotropy. Here, we derive the crustal anisotropy from the polarizations of the converted and multiple  $S$ -phases by including splitting times; therefore, a limited azimuthal event coverage is often sufficient. The approach can, thus, be applied to analyse data from temporary seismic stations. The consecutive application of the  $H$ - $\kappa$ -stacking algorithm inverting for an isotropic crust and its anisotropic extension (as presented here) including a possible layer dip yields increasingly complex models. We, therefore, compare stacks of moveout corrected waveforms for the different model results, to decide which degree of model complexity is necessary to best fit the data. We also introduce bootstrap statistics to estimate the stability of our result and search for ambiguities in the subsets of the receiver function data, which can be determined with a certain probability.

## METHOD

### Receiver function characteristics and alignment of crustal phases

Receiver functions are ideal to image seismic discontinuities. At such boundaries, incident  $P$  waves are partially converted to  $S$  waves. With each further interaction at a discontinuity the seismic phases are partially converted causing further reverberations recorded at the receiver (see Fig. 1a). In an isotropic case, without layer dip, the converted  $S$ -phases are only found on the radial (and vertical) components, while the transverse component remains free of energy. For an anisotropic regime or a dipping boundary, the waveforms are systematically changed. In the following, we assume hexagonal symmetry of the elastic properties with a horizontal symmetry axis, similar to previous studies. When propagating through the anisotropic medium, the converted shear waves will experience a split into two phases of differing velocity and perpendicular polarization according to the anisotropic fast and slow directions. For a model with a single anisotropic layer over an isotropic half-space, there are 20 phases with at least one  $S$ -wave leg (fast or slow) that arrive at the receiver (see Fig. 1b, Kaviani & Rumpker 2015). For the calculation of synthetic receiver functions in anisotropic layered structures, we use the code ‘raysum’ of Frederiksen & Bostock (2000), which also accounts for dipping interfaces. The exact location of the anisotropic layer(s) in the crust is generally not known due to

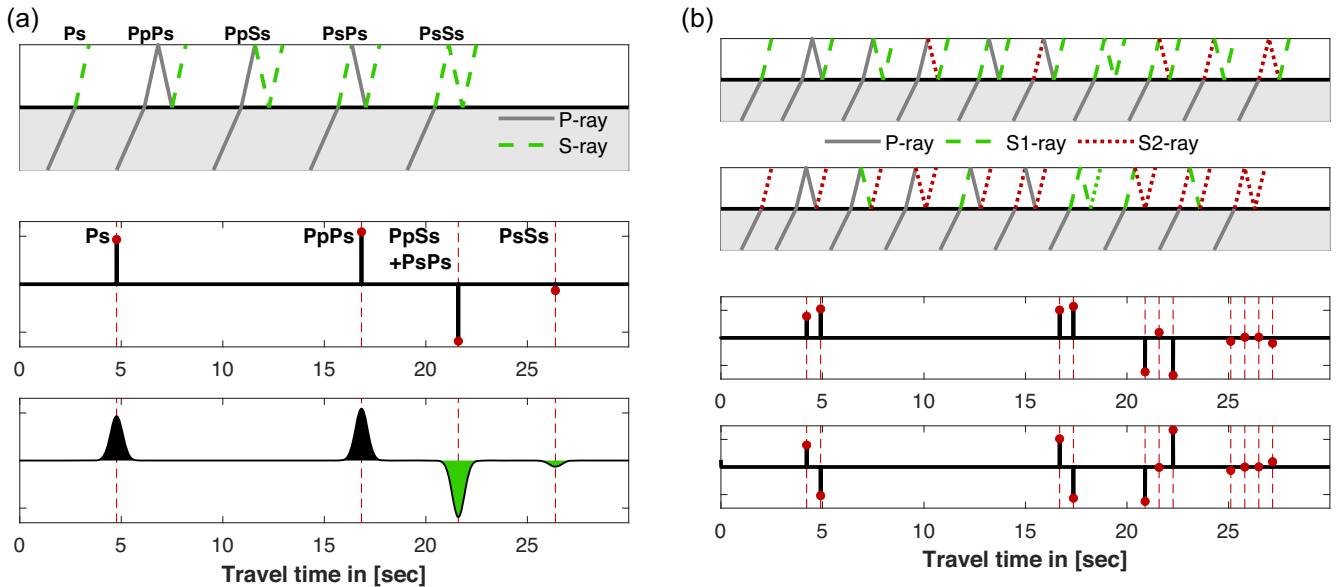


**Figure 1.** (a, top) Schematic illustration of possible ray paths for a first incoming  $P$ -wave converted at the crust–mantle boundary in the isotropic case.  $P$ -wave segments are shown in gray solid and  $S$ -wave segments in green dashed lines, respectively. The final segment for every ray path is a  $S$  wave. (a, middle) Corresponding delay times and amplitudes relative to the first arriving  $P$  wave. (a, bottom) The corresponding radial-component receiver function. The transverse component vanishes in the isotropic case. (b, top) Schematic illustration as in (a) but for an anisotropic crust.  $S$ -wave segments are now shown in green dashed line for  $S_1$  and red dotted line for  $S_2$ , respectively. (b, bottom) Corresponding lag times and amplitudes relative to the first arriving  $P$  wave for the anisotropic model with radial (top trace) and transverse (bottom trace) component amplitudes.

the various possible mechanisms responsible for anisotropy. We analyse the main converted phases at the Moho (e.g.  $Ps$ ,  $PpPs$ ) for the effect of anisotropy to characterize the bulk elastic properties of the crust. Any number of isolated anisotropic layers within the crust and/or at the surface will produce an effective anisotropy that affects the Moho converted  $S$ -phases and results in the split described above (see also Rumpker *et al.* 2014 and Fig 2). An anisotropic layer directly above the crust–mantle boundary will immediately lead to a separation of the converted shear wave into fast and slow phases propagating along (possibly rather) different ray paths, as shown, for example by Liu & Park (2017). This effect is amplified by the relatively strong velocity contrast at the Moho, whereas an anisotropic layer at (slightly) shallower depth has less effect on the ray paths. In this study, we focus on the bulk anisotropic properties of the crust and assume that anisotropy immediately above the Moho is less likely in comparison to scenarios where the anisotropic layer is located somewhere within the crust. We, therefore, consider a three-layer model consisting of an isotropic half space representing the upper mantle, an isotropic (infinitesimal thin) decoupling layer directly above the crust–mantle boundary (to account for the conversions), followed by an anisotropic layer, that represents the (bulk) properties of one or several anisotropic layers within the crust (for visualization see Fig. 2, left-hand side). In the following, we discuss the characteristics of receiver functions for different crustal models of this structure and describe an approach to align crustal phases from different events at the same receiver, while eliminating the effects of anisotropy and/or dipping velocity contrast (see Fig. 2). For an anisotropic crust with horizontal boundary, the crustal phases on the radial and transverse components show a characteristic azimuthal dependence. The energy of the fast and slow phases can be isolated when rotating the coordinate system into the fast/slow directions of the anisotropic medium (as described by orientation of the fast axis relative to north,  $\phi$ ). The phases can be shifted according to the split of the phases,  $\delta t_i$  (with  $i = Ps, PpPs, PsPs, PpSs, PsSs$ ), accumulated during propagation in the anisotropic medium and rotated back into the radial/transverse coordinate system to eliminate the anisotropic effect. As an example, we show in Fig. 2 this procedure starting with the radial and transverse receiver functions  $[R(t), T(t)]$ , rotated into the fast/slow coordinate system  $[F(t), S(t)]$ , corrected for the moveout  $[F(t - \delta t_i), S(t - \delta t_i)]$  and finally resulting in the alignment of the converted  $Ps$ -phase  $[R_c(t'), T_c(t')]$ , where we also consider the effect of moveout relative to a reference arrival time for an isotropic (reference) model and a ray parameter of  $0.05 \text{ s km}^{-1}$ . We show this alignment of the  $Ps$ -phase for different models for an anisotropic layer with fast, slow and plunging fast symmetry axis, as well as for a dipping boundary with horizontal symmetry axis and a layered crustal model with an anisotropic thin layer within an isotropic crust (Fig. 2, sketched in the left-hand column from top to bottom). A dipping boundary will cause a deflection of the ray. Therefore, the horizontal projection of the initial polarization (the backazimuth),  $\xi$ , for the converted shear waves is modified (rotated) according to,  $\xi + \delta\xi$ . This effect can dominate the azimuthal characteristics of the receiver functions. However, the fast and slow phases can still be isolated with a rotation into the fast and slow coordinate system described by the direction of the symmetry axis,  $\phi$ . An individual time-shift for each phase,  $\delta t_i$ , aligns all phases, when accounting for the anisotropic and path effects due to the dipping interface. The anisotropic effect will now only be eliminated, when rotating back into the polarization direction of the deflected ray,  $\xi + \delta\xi$ . A plunging symmetry axis of the anisotropic medium can also have effects on the crustal  $Ps$ -phase similar to a dipping layer (e.g. Savage 1998). However, in our models such a plunge has no significant effect on the crustal phases. This indicates that the observed effects of the previous studies only occur for cases in which the anisotropic layer is located

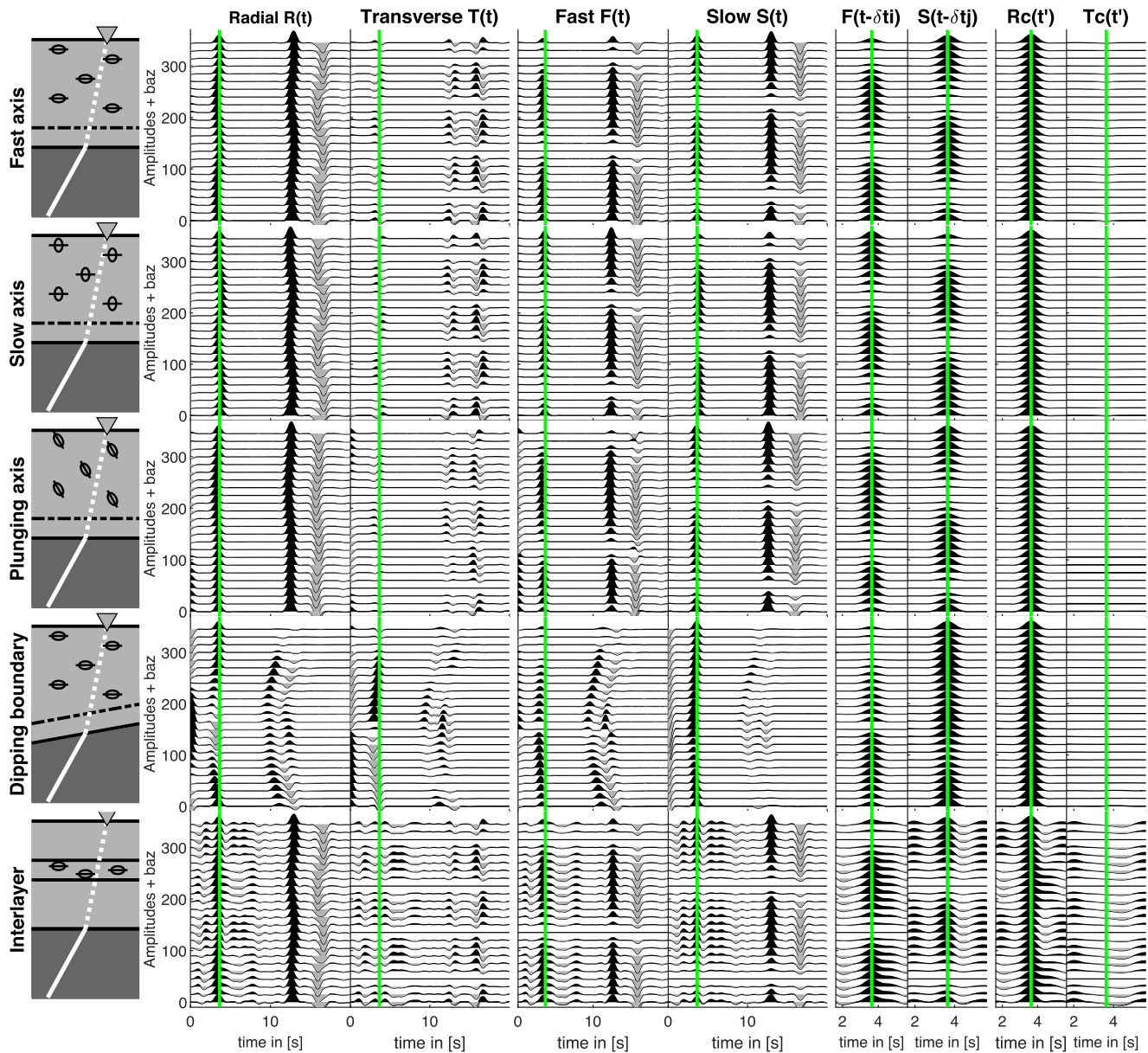


**Figure 2.** Procedure to align crustal phases in receiver functions for characteristic settings. (left-hand column) Sketch of the model used in the specific row. Each model is characterized by two layers representing the mantle (dark grey) and the crust (light grey) with an intermediate decoupling zone (separated by the dashed black line). The decoupling zone is isotropic and of infinitesimal vertical extension. It is used to decouple the effects of conversion at the Moho from the effects of anisotropy located at unknown depth range within the crust. The white line represents a ray from a teleseismic event traveling as  $P$  wave (solid line) through the mantle, converted at the crust–mantle boundary and arriving at the receiver (triangle) as a shear wave (dashed line). The ellipses indicate anisotropy with the symmetry axis (black bar) drawn along the long axis for the fast symmetry and short axis for the slow symmetry, respectively. The last row presents a model with a thin layer (5 km) of strong anisotropy (24 per cent) within an isotropic crust. The following columns show the corresponding radial and transverse receiver functions before and after rotation into the fast and slow coordinate system, respectively. The last two columns show a window around the  $Ps$ -phase after a time-shift to align the phases in the fast/slow coordinate system and rotated back into the radial/transverse coordinate system, respectively. The vertical solid green line is intended to visualize the moveout before and the alignment after the correction.

directly above the crust–mantle boundary (without the decoupling layer as used here). In the layered model we produce receiver functions for a thin anisotropic layer with large anisotropy of 24 per cent within an otherwise isotropic crust. While additional phases occur, due to the anisotropic velocity contrast between the isotropic and anisotropic medium, the main converted phases are clearly visible and the correction procedure shows that the transverse energy for the crustal phases can be removed. Only energy from phases arriving before and after the Moho-conversion remains visible in the corrected traces.

The alignment of the crustal phases allows a coherent stack, when summing up the corrected traces. We use this in the following to infer a stacking procedure searching for the properties of an anisotropic crustal model.

### Stacking algorithm and splitting correction scheme

In the procedure presented here, we modify the approach of Kaviani & Rumpker (2015), where the anisotropic as well as the structural properties of the crust are both determined from the stacking of receiver functions. Specifically, to infer the anisotropy, we also include the PpPs phase (in addition to the Ps phase) and apply techniques based on transverse-energy minimization as used in conventional shear wave splitting analysis. Furthermore, we simultaneously solve for structural and anisotropic properties, and also allow for a predefined layer dip.

First, we compute the relative arrival times and polarizations of the Ps- and PpPs-phases for the given model. As shown by Frederiksen & Bostock (2000) the arrival times for a layered medium are given by simple linear combinations

$$t = \sum_{i=1}^N q_i \cdot z_i, \quad (1)$$

where  $q_i$  is the vertical slowness component of ray segment  $i$ .  $z_i$  is the thickness of the layer  $i$  and  $N$  is the number of segments of the total ray path. The vertical slowness can be derived by solving the eigenvalue problem of the system matrix  $A$  (Woodhouse 1974), which describes the interaction of a seismic wave with an elastic medium. The main input parameters to build the system matrix are the horizontal slowness components,  $p_v$ , representing the incoming wave defined by the ray parameter,  $|p|$ , and the backazimuth,  $\xi$ , of a seismic source and the elastic properties of the medium, which we assume to be hexagonal anisotropic. Therefore, the density,  $\rho$ , the  $P$ -wave velocity,  $v_p$ , the ratio of the average velocities in the medium,  $\kappa = \frac{v_p}{v_s}$ , the percentage anisotropy,  $a$  and the direction of the symmetry axis relative to north,  $\phi$ , are convenient parameters to fully describe the system (Love 1920; Farra *et al.* 1991). The system matrix can also be used to derive reflection and transmission coefficients for the boundaries defining the layered media (Fryer & Frazer 1984; Guest *et al.* 1993). A detailed formulation is given in the supplements.

In our analysis, arrival times relative to the first arriving  $P$  wave, lag times ( $\Delta t_i$ , with  $i$  describing the phases  $Ps_1$ ,  $PpPs_1$ ,  $Ps_2$  and  $PpPs_2$ ), are required. The subscripts to discriminate the fast and slow travelling shear phases in an anisotropic medium are only used if the discrimination is necessary. As described above, we consider the crust as a single anisotropic layer above an isotropic half space with an isotropic decoupling layer,  $\delta$ , of infinitesimal thickness,  $\delta H$ , where  $\delta H \ll H$ . In view of eq. (1), the time difference between the first converted  $S$  and the direct  $P$  wave then is given by

$$\Delta t_{Ps} = (q_S^U - q_P^U) \cdot H + (q_{S,\delta}^U - q_{P,\delta}^U) \cdot \delta H \cong (q_S^U - q_P^U) \cdot H, \quad (2)$$

where  $D$  and  $U$  denote downward and upward travelling waves,  $P$  and  $S$  denote the wave type and  $H$  the thickness of the crust. For the multiple PpPs, we obtain

$$\begin{aligned} \Delta t_{PpPs} &= (q_P^U + q_P^D + q_S^U - q_P^U) \cdot H + (q_{(P,\delta)}^U + q_{(P,\delta)}^D + q_{(S,\delta)}^U - q_{(P,\delta)}^U) \cdot \delta H \cong \\ &= (q_P^U + q_P^D + q_S^U - q_P^U) \cdot H, \end{aligned} \quad (3)$$

or

$$\Delta t_{PpPs} \cong (q_P^D + q_S^U) \cdot H, \quad (4)$$

The polarizations can be obtained by combining the appropriate reflection,  $R$ , and transmission,  $T$ , coefficients (Fryer & Frazer 1984; Guest *et al.* 1993; Frederiksen & Bostock 2000) and by including the effect of the free surface,  $w$ ,

$$\mathbf{u}_{P(pP)k} = \mathbf{w}_k \prod_{l=1}^N \mathbf{X}_k^l \quad (5)$$

with

$$\begin{aligned} \prod_{l=1}^N \mathbf{X}_k^l &= \mathbf{T}_{UPs}^\delta \mathbf{T}_{USk} \rightarrow N = 2; k = S_1, S_2 \\ \prod_{l=1}^N \mathbf{X}_k^l &= \mathbf{T}_{UPp}^\delta \mathbf{T}_{UPp} \mathbf{R}_{DPp}^0 \mathbf{T}_{DPp}^\delta \mathbf{R}_{UPs}^\delta \mathbf{T}_{USk} \rightarrow N = 6; k = S_1, S_2. \end{aligned} \quad (6)$$

The first statement of eq. (6) describes the computation for the recorded Ps-phase at the receiver with a conversion of the arriving  $P$  wave at the decoupling zone (indicated by superscript  $\delta$ ) to an  $S$  wave described by the transmission coefficients in matrix  $\mathbf{T}_{UPs}^\delta$  followed by the immediate transmission into the anisotropic crustal layer, where the split into a fast and slow  $S$ -phase occurs according to the coefficients of  $\mathbf{T}_{USk}$ . The second statement considers the corresponding transmissions and reflections for the PpPs-phase. Here the first transmissions only consider the  $P$  wave, which is then reflected at the surface (indicated by the superscript 0) according to the reflection coefficients of  $\mathbf{R}_{DPp}^0$ . The conversion to an  $S$  wave occurs at the reflection from the crust–mantle boundary into the decoupling zone according to  $\mathbf{R}_{UPs}^\delta$ , while the converted  $S$  wave again experiences a split when transmitted into the anisotropic crustal layer.

In the case of a dipping boundary, which can be defined by a strike direction and a dip from the horizontal, every incoming ray has to be rotated into a coordinate system, where the velocity boundary is horizontal, resulting in a new horizontal slowness and accordingly a new system matrix for a likewise rotated elasticity tensor. Therefore, reflection and transmission coefficients, as well as the vertical slowness have to be derived for every interaction of a phase with the rotated interface.

**Table 1.** Variable and predefined parameters to calculate delay times and amplitudes for an anisotropic model, with a possible layer dip defined by strike and dip ( $\alpha, \beta$ ) and plunge of the symmetry axis ( $\theta$ ). The ray parameter and backazimuth ( $|\mathbf{p}|, \xi$ ) are defined by the event location. The system matrices for the lower crust  $A_{lc}$  and mantle  $A_{hs}$  have to be rotated for interactions of the ray path with the dipping interface denoted by the superscript  $R$ . The system matrix of the crust  $A_C$  is constructed from predefined and variable parameters.  $H$  denotes the thickness of the crustal layer.

$p_v$	$A_{hs}$	$A_{hs}^R$	$A_{lc}$	$A_{lc}^R$	$A_C$	$H$
$ \mathbf{p}  \xi$	$\rho_{hs} v_{P_{hs}}$ $v_{S_{hs}}$	$\alpha \beta$	$\rho_{lc} v_{P_{lc}}$ $v_{S_{lc}}$	$\alpha \beta$	$\rho_c v_{P_c}(\theta)$ $\kappa a \phi$	$H$
Event	Preset		Preset		Variables	Variable

**Table 2.** List of parameters used to calculate the models (I–V).

	Fixed parameters		Lower crust				Bulk crust		
	Half space								
$\rho [\frac{kg}{m^3}]$		3500				2900		2850	
$v_P [\frac{m}{s}]$		8100				6800		6300	
$v_S [\frac{m}{s}]$		4500				3900		$v_P/\kappa$	
	Variable parameters								
	$H$ [km]		$\kappa (v_{S_c})$		$a$ [per cent]	$\varphi$ [°]	$\theta$ [°]	$\alpha$ [°]	$\beta$ [°]
Model I	30		1.73		4	45	0	0	0
Model II	30		1.73		−4	45	0	0	0
Model III	30		1.73		4	45	60	0	0
Model IV	30		1.73		4	45	0	235	20
	$H_1$ [km]	$H_2^A$ [km]	$H_3$ [km]	$\kappa (v_{S_c})$	$a$ [per cent]	$\varphi$ [°]	$\theta$ [°]	$\alpha$ [°]	$\beta$ [°]
Model V	10	5	15	1.73	24	45	0	0	0

To derive the arrival times and polarizations of the anisotropic Ps- and PpPs-phases, the parameters have to be set as shown in Table 1. In our study, we only search for the percentage crustal anisotropy,  $a$ , the orientation of the symmetry axis,  $\phi$ , the ratio of average crustal velocities,  $\kappa$ , and the depth extent of the crust,  $H$ . While the horizontal slowness and the backazimuth are given by the event location, the remaining parameters, for example density of the half space and crust, as well as isotropic average  $P$ - and  $S$ -wave velocities, have to be predefined using appropriate values for different geological settings. Specifically, this applies to the average (bulk) values for the crust,  $\rho_c$ ,  $v_{P_c}$ , for the lower crust,  $\rho_{lc}$ ,  $v_{P_{lc}}$ ,  $v_{S_{lc}}$ , (to be used when calculating the transmission at the decoupling zone) and for the underlying mantle,  $\rho_{hs}$ ,  $v_{P_{hs}}$ ,  $v_{S_{hs}}$ . Exemplary values as used in this study are listed in Table 2. Most of the parameters, for example densities and velocities in the half space and the decoupling zone, only affect the magnitude of the absolute amplitudes and have negligible influence on the inversion itself, whereas the  $P$ -wave velocity of the crust,  $v_P$ , affects the arrival times of relevant phases. As lag times are less sensitive to the  $P$ -wave velocity changes, we choose a constant value of  $6300 \text{ m s}^{-1}$  for all models. The following steps describe the analysis for an anisotropic horizontal crustal layer.

(i) We first calculate the phase-related lag times  $\Delta t_i$  and particle motion  $\mathbf{u}_i$  for realistic ranges of parameters ( $H, \kappa, a, \phi$ ) yielding

$$\Delta t_i = \Delta t_i(H, \kappa, a, \phi), \quad \mathbf{u}_i = \mathbf{u}_i(H, \kappa, a, \phi) \quad (7)$$

for the phases  $i = P_{S_1}, P_{S_2}, PpPs_1, PpPs_2$ .

(ii) In the second step, we obtain the corresponding horizontal polarizations from the radial ( $RRF$ ) and transverse receiver functions ( $TRF$ ) at the calculated times

$$\mathbf{x}_i = [RRF(\Delta t_i(H, \kappa, a, \phi)), TRF(\Delta t_i(H, \kappa, a, \phi))]^T, \quad (8)$$

where  $\mathbf{x}_i$  are the amplitudes found in the radial and transverse receiver functions at the computed times  $\Delta t_i$  for the phase  $i$ .

(iii) The receiver functions are rotated into the (assumed) fast-slow coordinate system. The rotation angle corresponds to the polarization angle of the fast phases  $\psi$  in the horizontal plane, which can be derived from the particle motion  $\mathbf{u}_{P_{S_1}}$  for each parameter set of ( $H, \kappa, a, \phi$ ), yielding

$$\mathbf{x}_i \xrightarrow{\psi(H, \kappa, a, \phi)} \mathbf{x}_i^{fs}, \quad (9)$$

where the superscript  $fs$  denotes the amplitude vector in the fast/slow coordinate system.

(iv) Amplitudes of the fast and slow phases are taken at their respective times and combined to correct for the effect of the time-shift due to anisotropy

$$\mathbf{x}_{P_{S_1}}^{fs'} = \begin{pmatrix} x_{P_{S_1}}^f \\ x_{P_{S_1}}^s \end{pmatrix}, \quad \mathbf{x}_{PpPs_1}^{fs'} = \begin{pmatrix} x_{PpPs_1}^f \\ x_{PpPs_1}^s \end{pmatrix}, \quad (10)$$

where  $f$  and  $s$  describe the fast and slow components of the amplitude vector  $\mathbf{x}_i^{fs}$ , respectively. The superscript  $'$  denotes amplitude vectors,  $\mathbf{x}$ , for which the time-shift has been applied.

(v) The corrected phases are then rotated back into the radial and transverse coordinate system,

$$\mathbf{x}_i^{fs'} \xrightarrow{\chi_i} \mathbf{x}'_i, \quad (11)$$

with the rotation angle  $\chi_i = -\psi$  for horizontally layered models. In the case of a dipping layer, the rotation angle for eliminating the transverse energy differs from the horizontal polarization as mentioned before. In this case the new angle,  $\chi_i$ , for the rotation can be found from the polarization of the time-shifted Ps-phase,  $\mathbf{u}_{Ps}^{fs'}$ , and PpPs-phase,  $\mathbf{u}_{PpPs}^{fs'}$ , for which the rotation and recombination steps have been performed likewise.

(vi) We sum up the corrected amplitudes on the radial component minus the absolute transverse amplitudes yielding individual energy stacks for each event. The individual stacks are then summed up for all  $M$  events recorded at the station:

$$F(H, \kappa, a, \phi) = \sum_{i=1}^M \left[ x_{Ps}^{r'} - |x_{Ps}^{t'}| + x_{PpPs}^{r'} - |x_{PpPs}^{t'}| \right], \quad (12)$$

where the superscripts  $r$  and  $t$  denote the radial and transverse component of the corrected amplitude vector  $\mathbf{x}'_i$ , respectively. We additionally introduce weighting factors to allow for a manual or automatic quality control. Constant weights,  $c_i$ , as proposed by Zhu & Kanamori (2000), allow for a relative weighting of the phases. In the following, we use the values 0.7 and 0.3 for the Ps and PpPs phases, respectively. The semblance function of Eaton *et al.* (2006),  $S_i$ , is used to quantify the coherency of the stack for the phases  $i = Ps, PpPs$  given a particular parameter combination  $(H, \kappa, a, \phi)$ . With these additions (in view of 12) the summation is written as

$$F(H, \kappa, a, \phi) = \sum_{i=1}^2 S_i(H, \kappa, a, \phi) \sum_{j=1}^M c_j \left[ x^{r'}(\Delta t_{ij}) - |x^{t'}(\Delta t_{ij})| \right], \quad (13)$$

where the semblance is defined as

$$S_i(H, \kappa, a, \phi) = \frac{\left( \sum_{j=1}^M [x^{r'}(\Delta t_{ij}) - |x^{t'}(\Delta t_{ij})|] / M \right)^2}{\sum_{j=1}^M [x^{r'}(\Delta t_{ij}) - |x^{t'}(\Delta t_{ij})|]^2 / M}. \quad (14)$$

(i) For the true parameters  $(H, \kappa, a, \phi)$  of the crust, the rotation is expected to minimize the absolute transverse receiver-function amplitude and maximize the radial amplitude. The maximum of the stacking function  $F(H, \kappa, a, \phi)$  leads to the parameters  $H_0, \kappa_0, a_0$  and  $\phi_0$  that best fit the observed data.

## Synthetic tests

We perform extensive tests for synthetic models (with one anisotropic layer above an isotropic half space and an intermediate decoupling zone, as described above) to estimate the stability of our approach in various scenarios. We present four models of crustal anisotropy with (I) moderate strength of anisotropy, (II) a slow symmetry axis instead of a fast axis, (III) a plunge of the fast symmetry axis and (IV) the same as model I with an additional (predefined) dip of the layer boundary given by the strike direction  $\alpha$  and the dipping angle  $\beta$ . To further test the validity of our approach, we also test a model characterized by a thin layer of strong anisotropy within an isotropic crust (V). The parameters used for calculating the models I–V are listed in Table 2. We produce the synthetic traces using a MATLAB<sup>®</sup> (Mathworks, Inc., Natick, MA, USA) version of the code ‘raysum’ (Frederiksen & Bostock 2000). The models are used to assess how accurately we can resolve the parameters  $H, \kappa, a$  and  $\phi$  of the layer in different settings. For the initial tests without noise we calculate synthetic traces for the ray parameters 0.05, 0.06, 0.07 and 0.08  $\text{km}^{-1}$ . The backazimuths of the events for each ray parameter are varied by  $15^\circ$  over the complete azimuthal range. More realistic conditions, including noise and random event distribution, will be considered in a section below. The introduced stacking approach is applied for different model classes with growing degree of complexity. We consider three types of solutions or model classes: the first is derived under the assumption of isotropy (ISO) using the  $H$ – $\kappa$ -stacking algorithm of Zhu & Kanamori (2000); for the second solution, we apply the anisotropic algorithm without layer dip with a fast symmetry axis (ANI) and a slow symmetry axis (only for model II, ANI-S); for the third solution, we include a predefined layer dip (only for model IV, ANID).

## Anisotropic stacking for different model classes

In the first test based on model I, we choose anisotropy of 4 per cent for both the  $P$ - and  $S$ -wave velocities with a (horizontal) fast axis of  $45^\circ$ . We first apply the classical  $H$ – $\kappa$ -stacking algorithm of Zhu & Kanamori (2000) that assumes an isotropic crust (see Fig. 3, ISO). This results in a layer thickness of 30.9 km and a velocity ratio of 1.69, slightly off the real model values. We then perform the described anisotropic stacking approach by summing up the amplitudes for corrected Ps- and PpPs-phases [radial minus transverse component, see eq. (13)], where the transverse energy should vanish if corrected with the true anisotropic parameters. As the stacking function now depends on four

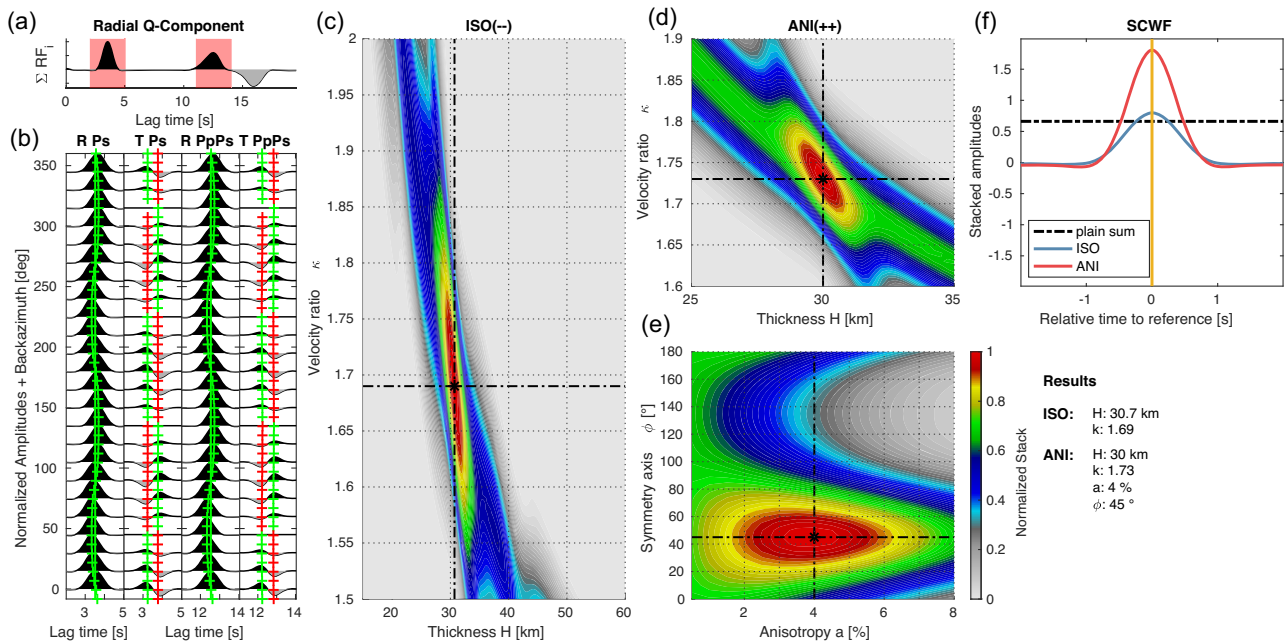


**Figure 3.** Stacking analysis for synthetic data of model I. (a) Sum trace over all radial receiver functions. (b) Azimuthal stacks of the radial and transverse receiver functions are shown windowed around the Ps- and PpPs-phase (marked red in a). The following columns show the stacking function for the isotropic (ISO, c) and anisotropic analyses (ANI, d–e), respectively. The corresponding results are marked by the crossed lines and the corresponding lag times are marked in the azimuthally sorted receiver functions as solid line (indicated in the title as ‘—’) for the isotropic and marked by pluses (indicated in the title as ‘+++’) for the anisotropic solution. Red and green colors indicate the expected sign of the amplitude for this arrival. (f) Moveout corrected stack of waveforms (SCWF) for the two solutions in comparison to a plain stack of the receiver functions (black dashed line). The maximum with the highest magnitude corresponds to the most coherent stack of the Ps- and PpPs-phase. Detailed results of the analyses (indicated by ISO and ANI) are given in the lower right corner

parameters, we show 2-D cuts through the maximum of the stacking function, for the  $H$ - $\kappa$ - and  $a$ - $\phi$ -planes (see Fig. 3, ANI). The anisotropic approach yields the exact model parameters ( $H = 30$  km,  $\kappa = 1.73$ ,  $a = 4$  per cent and  $\phi = 45^\circ$ ). With analysis of model V we test if the approximation of one layer anisotropy is valid for an intercrustal anisotropic layer at arbitrary location. While there appear additional phases in the receiver functions, due to conversions at the interfaces between the strong anisotropic ( $a = 24$  per cent) and isotropic layers, the result of the stacking analysis are in agreement with the average values for the bulk crust, which are the same as for model I (see Fig. 4).

To determine which model class (ISO or ANI) fits the data best (or which degree of complexity is required to explain the data), it is necessary to check the plausibility of the corresponding results. We, therefore, perform a stacking of moveout corrected waveforms by including both the Ps- and PpPs-phases: First, we correct for the anisotropic effects (and layer dip, if present) and then shift all phases to a reference time according to the specific model class and the results ( $H_0$ ,  $\kappa_0$ ,  $a_0$ ,  $\phi_0$ ) for the crust obtained from the stacking approach. In the second step, the time-shifted radial component waveforms of the Ps- and PpPs-phases ( $RRF'_{Ps,i}$ ,  $RRF'_{PpPs}$ ) are summed up, while also accounting for the remaining energy on the transverse component

$$SCWF(H_0, \kappa_0, a_0, \phi_0) = \sum_{i=1}^M \left[ \sqrt{1 - \frac{ET_{Ps,i}}{ER_{Ps,i}}} \cdot RRF'_{Ps,i} + \sqrt{1 - \frac{ET_{PpPs,i}}{ER_{PpPs,i}}} \cdot RRF'_{PpPs} \right], \quad (15)$$

where  $ET$  and  $ER$  denote the transverse and radial energy of the particular phase, respectively. An explanation for the factors (roots) in eq. (15) can be found in the supplements. This summation of corrected waveforms (SCWF) allows to identify the ‘most coherent’ stack (and, therefore, the most likely model class) by comparing the maxima obtained for different model classes.

When applying the moveout correction to the receiver-functions generated for model I, it becomes evident that accounting for anisotropy leads to a more coherent stacked signal in comparison to an isotropic model assumption (see Fig. 3). As the transverse energy is considered in the stacked moveout corrected waveforms (SCWF), the coherency increases due to the correction for the anisotropic effect before stacking the waveforms. This also indicates that, for an isotropic model, considering spurious anisotropy in the SCWF would lead to energy mapped onto the transverse component associated with a decrease of the coherency. Therefore, the SCWF provides a valid estimation of the model class to best explain the data. We also use this coherency check to compare the results of all analysed classes of our models, to confirm that a growing degree of complexity leads to a better fit to the data. A comparison of the SCWF after analysing the receiver functions of model IV dominated by a layer dip of  $20^\circ$  shows that a consideration of the layer dip is necessary to improve the coherency when stacking the phases (see Fig. 5).

Depending on the tectonic domain, layer dip may be important. Our tests show that a layer dip should be taken into account to derive meaningful results for the crustal parameters, if its effect is large enough to affect the appearance of the receiver functions. Contrary to the distinct improvement of the coherency for model IV, when the layer dip is considered, the comparison of the results for a slow symmetry

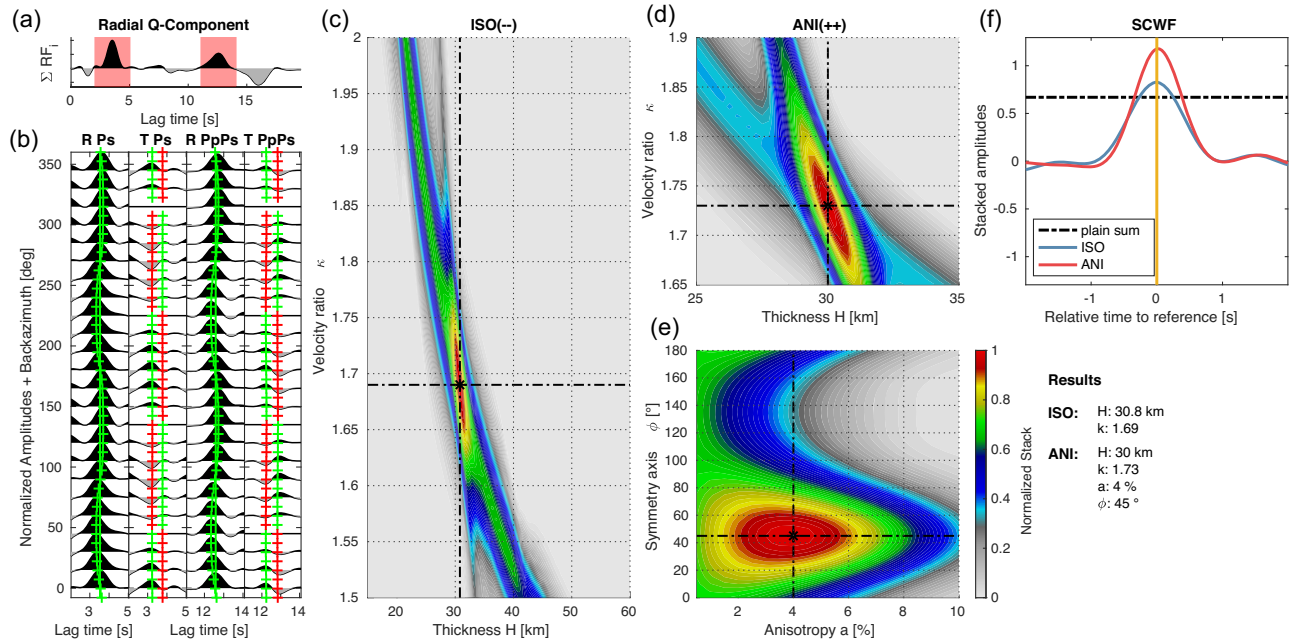


**Figure 4.** Same as Fig. 3, but for model V with a thin layer of strong anisotropy within an isotropic crust. The good agreement with the results from analysis of model I (see Fig. 3) supports the validity of approximating the elastic properties of the crust by a single layer of uniform anisotropy distributed over the entire crust.

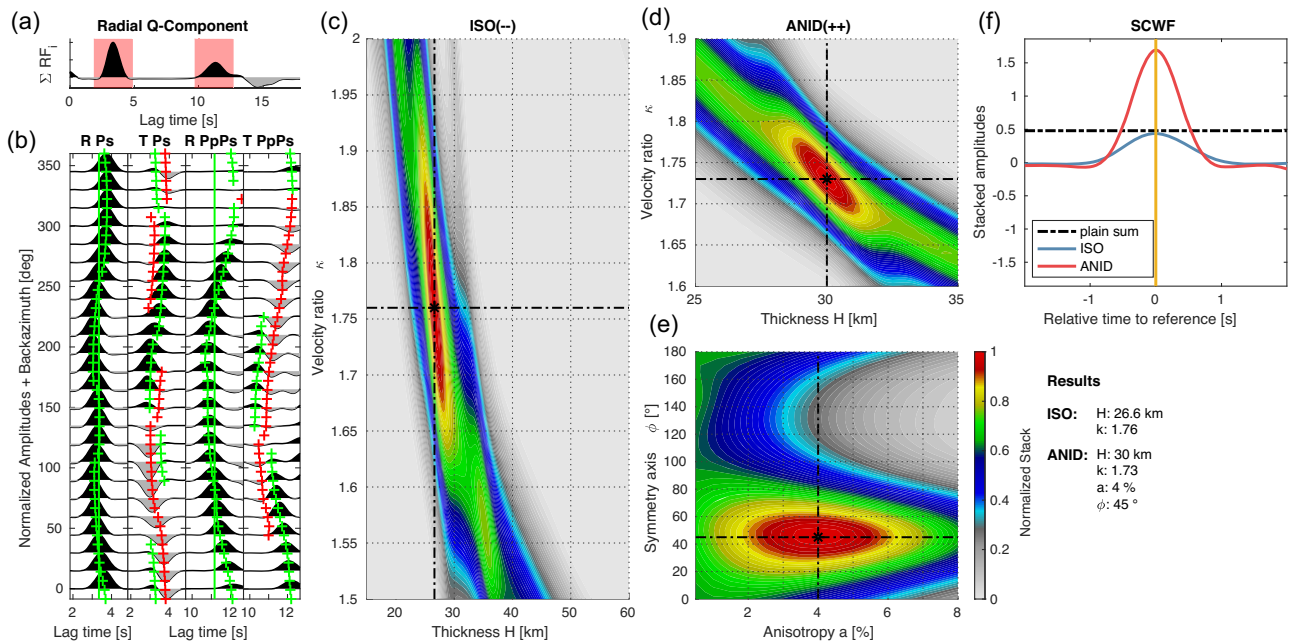


**Figure 5.** Same as Fig. 3, but for model V. (d)–(e) Stacking function for an anisotropic analysis considering the layer dip (ANID) of  $20^\circ$ . The large difference in the stack of the moveout corrected waveforms confirms the necessity of including available information on layer dip in the analysis procedure.

model (II) under the assumption of a fast or a slow symmetry axis (ANI-S) leads to the same coherency in the stacked amplitudes (see Fig. 6). This indicates that it is not possible to differentiate between the nature of elastic symmetry from the data alone. Nevertheless, at the same time  $\kappa$  is highly overestimated for the incorrect symmetry assumption, just as in the isotropic analysis. Therefore, if petrological information for the area of interest is available, which allows to estimate  $\kappa$ , it can help to choose the correct type of symmetry axis (see also Hammond 2014). In general, to interpret the origin of the anisotropy derived from receiver function analysis, the type of symmetry (fast or slow) has to be estimated in view of geological or petrological conditions, either prior to analysis or when comparing the results for both cases.

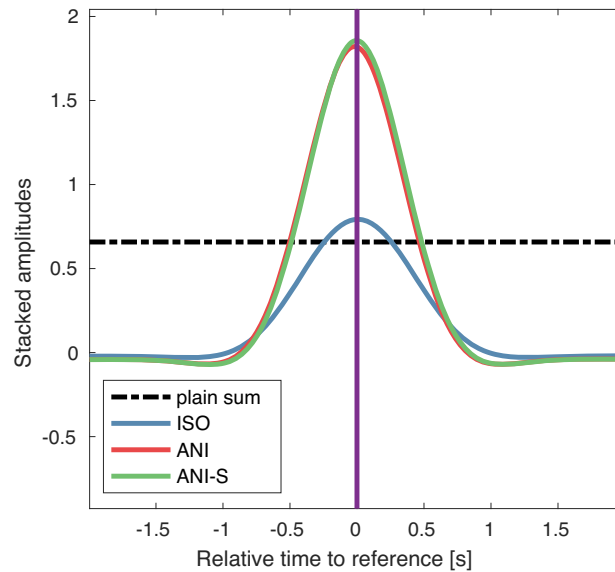


**Figure 6.** Comparison of moveout corrected stacks of waveforms (SCWF) from model II for solutions from an isotropic (ISO), anisotropic analysis assuming a fast axis (ANI) and anisotropic analysis assuming a slow symmetry axis (ANI-S). The almost equal magnitude of the stacks for the two anisotropic solutions point to the ambiguity of the procedure. A differentiation between fast and slow symmetry axis is not possible.

### Noise contamination—bootstrapping statistics

All tests are also performed for a more realistic situation by introducing a randomized distribution of the events, a complex signal and realistic noise conditions. We randomly choose 100 values for the ray parameter between  $0.0405$  and  $0.095 \text{ s km}^{-1}$  and for the backazimuth between  $0^\circ$  and  $360^\circ$ . We convolve the synthetic seismograms with a cosine-type signal with dominant frequencies of  $0.05$  and  $0.2 \text{ Hz}$  to replicate the source pattern of a teleseismic signal. To simulate realistic noise conditions, we choose a time window (with length of the synthetic traces) of pre-event noise from the broadband station TNS of the German regional network (network code GR). The maximum absolute amplitude of the noise added to the traces is normalized to be equivalent to a signal to noise ratio of  $1.2$  on the radial component. We compute the receiver functions using the water-level deconvolution (Langston 1979) with minimum amplitude of  $0.005$  normalized to the maximum amplitude in the frequency spectrum after filtering the traces with a second-order Butterworth filter and cut-off frequencies of  $0.05$  and  $0.5 \text{ Hz}$  (see also Fig. S4 in the supplements).

The plain sum of the receiver functions for model I still provides a relatively clear image of the converted and multiple phases (Fig. 7). Therefore, the (isotropic)  $H$ - $\kappa$ -stacking algorithm shows almost the same result as for the uncontaminated model I and the anisotropic analysis also yields similar model parameters with minor variations (compare Fig. 7 with Fig. 3, ISO and ANI). To assess the stability of the results and to derive a confidence region for the parameters obtained from the grid search, we follow the bootstrap method (Efron 1979) by randomly drawing the same number of traces with replacement from the original data set. For the new data set the grid search is repeated. The procedure is iterated 800 times. The best model parameters and the corresponding error are estimated by fitting a normal distribution which yields the mean and the standard deviation  $\sigma$ . From the  $2\sigma$ -interval around the mean a certainty range of 95.45 per cent is derived. This probability estimate assumes that the given model parameters are correct and that the model class used for the analysis is representative of the real structure. Therefore, the error derived from the bootstrapping only accounts for the data uncertainty based on a particular model. Assumption of  $P$ -wave velocity and layer dip in the input model may lead to additional uncertainties, which are not reflected in the bootstrap. The sensitivity of the results on these parameters are well described in previous studies (see also Wölbern & Rumpker 2017 for the sensitivity on  $P$ -wave velocity and Lombardi *et al.* 2008 on dipping effects) and require a careful choice of the input parameters. This approach of error estimation can be used for any kind of stacking approach relying on a considerable amount of events. Ambiguities can be resolved for a random stack of subsets of object functions (e.g. stacking functions in receiver function studies, energy grids or error surfaces, when analysing shear-wave splitting), as it is done here. The distribution of the results for the noise-contaminated model I shows characteristics of a normal distribution, confirming that the mean and the standard deviation can be used as a reliable estimate of error.

We apply the same analysis to model III with a plunging symmetry axis of  $60^\circ$  (see Fig. 8). While the layer thickness and velocity ratio are determined very well, the main effect of the plunge is a decrease of the measured anisotropy  $a = 1.7 \pm 0.7$  per cent. Hence the uncertainty to constrain the fast-axis direction also increases. Generally, this test confirms that a plunging axis has a negligible influence on the results obtained for the parameters  $(H, \kappa, \phi)$ , while the strength of the anisotropy is significantly underestimated. Thus, in view of the application to real data, when assuming a hexagonal symmetry, the true anisotropy in the crust may be higher, if the plunge of the symmetry axis is not accounted for.

As a final example, using synthetic data, we generated receiver functions for model I with an event distribution reflecting the situation of a real data case (based on receiver functions for station TORNY, also shown in the next section) with a limited backazimuthal range

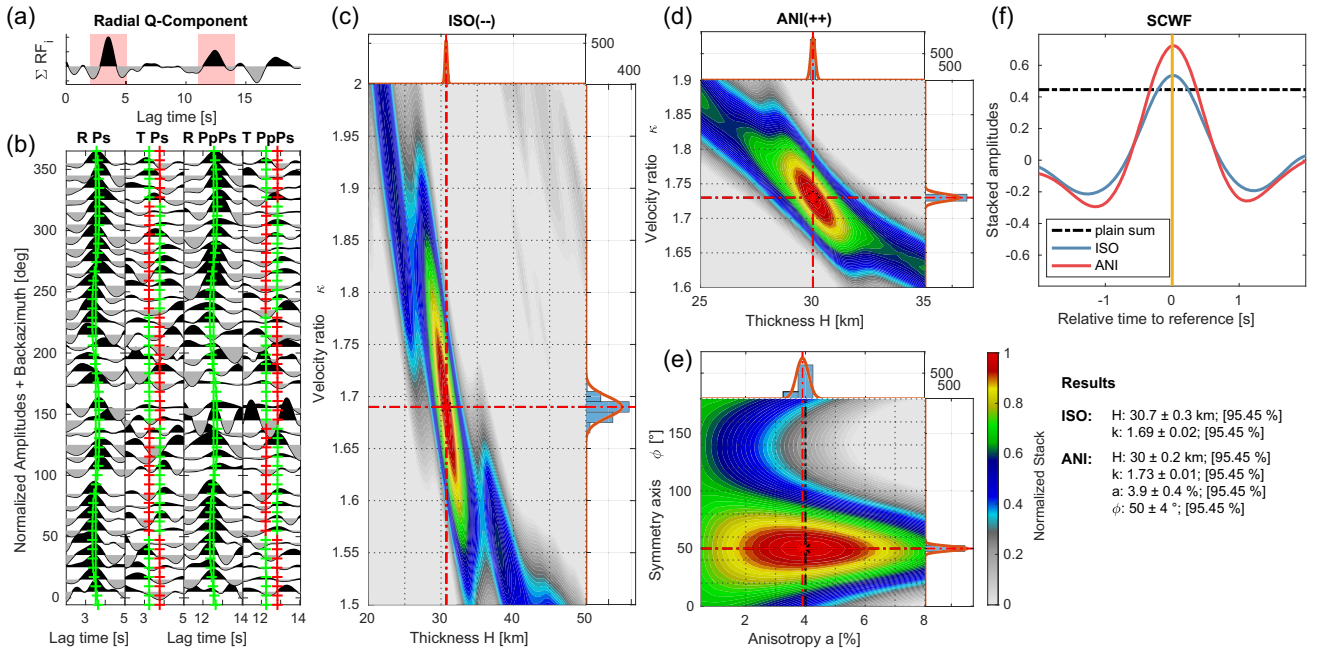


**Figure 7.** Same as Fig. 3, but for noise-contaminated traces of model I and a randomized event distribution. The bar plots attached to the axes of the stacking functions (c–e) present the results from the bootstrapping. The solid line is a fit of a Gaussian function to the distribution normalized by the number of fitted elements. The mean and the  $2\sigma$ -interval from the standard deviation lead to the results in the right-hand column. The  $2\sigma$ -interval corresponds to the probability of 95.45 per cent of all measurements of the fitted group to be located within the error bounds.

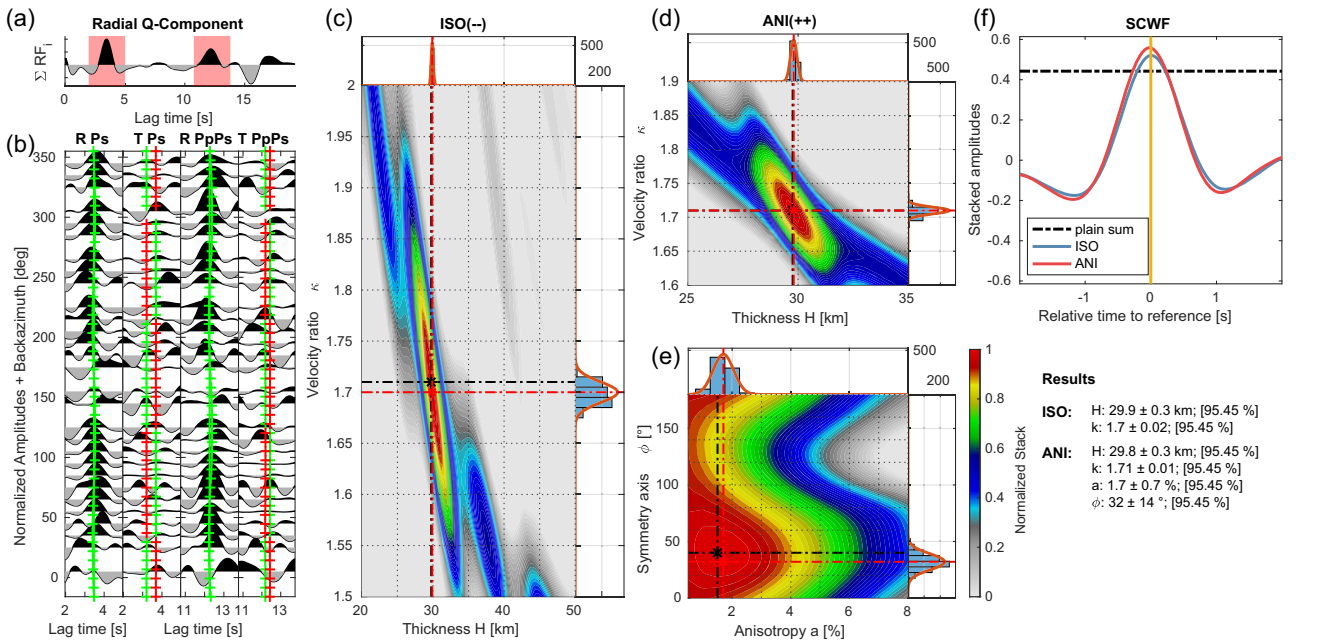


**Figure 8.** Same as Fig. 7, but for an analysis of model III. As the plunge of the symmetry axis decreases the measured magnitude of the anisotropy and the uncertainty for determining the fast axis increases (e). Simultaneously, the stacks of the moveout corrected waveforms (f) for the isotropic and anisotropic solution converge.

of  $0$ – $120^\circ$ . This allows to test the applicability of the method in temporary deployments with limited azimuthal event coverage. Here, the isotropic analysis underestimates  $\kappa$  relative to the case of a full azimuthal range (see Fig. 7), which might be expected, as the azimuthal moveout from the anisotropic effect is not compensated completely from the averaging of the isotropic stacking (see Fig. 9). However, the anisotropic stacking reproduces the model well for both the structural and the anisotropic parameters.

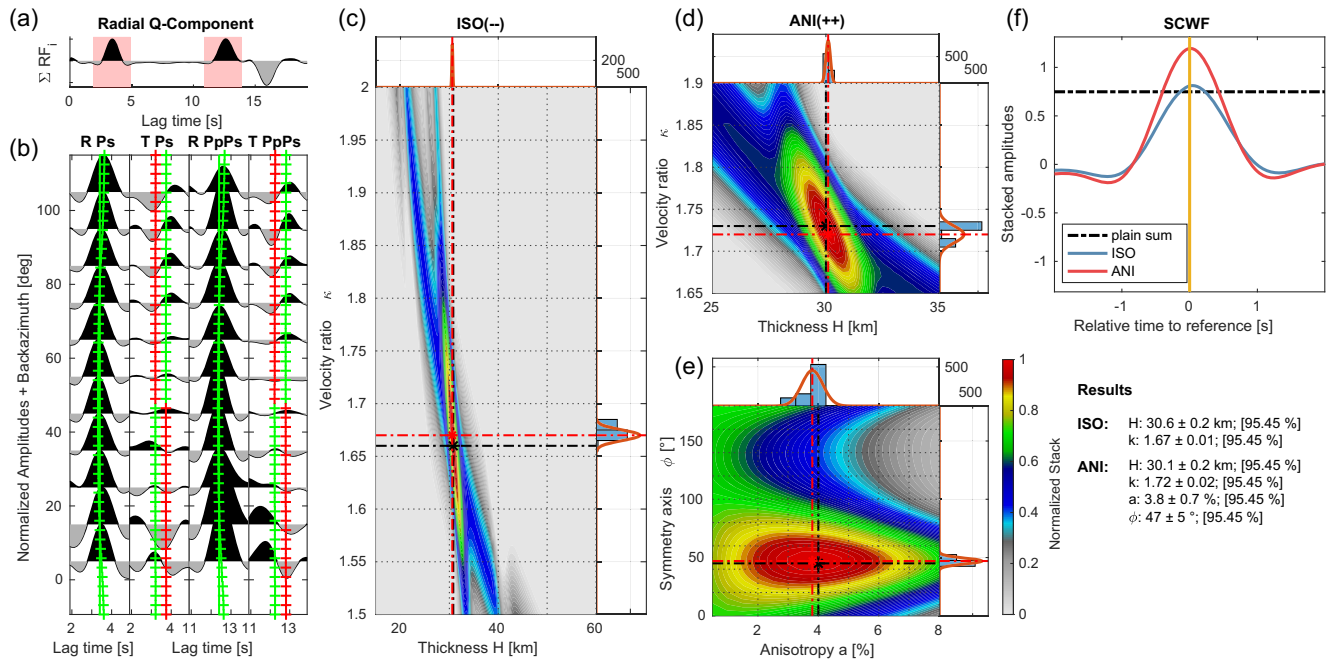


**Figure 9.** Same as Fig. 7, but for a realistic event distribution (relative to station TORNY for events between 2016 and 2017 and SNR above 1.5) reflecting a temporary and azimuthally restricted data set (only events between  $0^\circ$  and  $120^\circ$  backazimuth are considered). The good recovery of the model parameters supports the applicability of the method to data from temporary deployments.

### Application to real data

To test the stability and applicability of the proposed method, we consider real-data examples for three permanent seismic stations. The data for two of them (LSA located in Lhasa/Tibet is part of the New China Digital Seismograph Network and GRFO located in southern Germany is part of the Global Seismograph Network) have been analysed previously by Kaviani & Rumpker (2015). This allows for a direct comparison of the two approaches and for discussing the stability of the results. We also apply our method to data of the station TORNY located in Switzerland within the European Alps which is part of the Switzerland Seismological Network. The data for the three stations is accessible from IRIS. To obtain receiver functions, we selected teleseismic events from sources in an epicentral distance range between  $25^\circ$  and  $95^\circ$ . The traces are windowed 10 s before and 180 s after the arrival of the  $P$  wave and rotated from the ZRT-system to the ray-based LQT-system, where the L-component points to the expected propagation direction of the  $P$  wave. Q is aligned with the SV-movement and T with the SH-movement of the seismic phases. Traces with a SNR of less than 1.2 on the radial component are discarded. A bandpass filter with corner frequencies of 0.05 and 0.5 Hz is applied to reduce high-frequency noise. The receiver functions are derived using the water-level deconvolution (Langston 1979) as described above for the noise contaminated synthetic data. We obtain 2771 receiver functions for station LSA, 1310 for station GRFO and 725 for station TORNY. As for the synthetic data, we first apply the isotropic  $H$ - $\kappa$ -stacking to identify the Ps-phase converted at the Moho. Then an anisotropic stacking, assuming a fast symmetry axis, is applied. For the station TORNY a Moho dip is also considered. The bootstrapping allows us to constrain the stability and uniqueness of the results. Finally, a moveout correction is applied and the Ps- and PpPs-phases are stacked. The coherency of the stack, as determined from the maximum amplitude of the SCWF (see eq. 15) at a given reference time, is used to decide which model class, the isotropic (ISO), anisotropic (ANI) or anisotropic including dip (ANID), best explains the data.

For GRFO (see Fig. 10), the early peak in the receiver functions at  $\sim 0.7$  s indicates a strong shallow velocity contrast within the crust caused by a thick sedimentary layer (Krüger & Weber 1992; Kind *et al.* 1995). The converted phase at the Moho arriving at  $\sim 4$  s and the corresponding first reverberations at  $\sim 13.4$  s can be identified quite clearly. The isotropic stacking analysis with a search for the Moho depth ranging from 20 to 60 km and the bootstrapping lead to  $H = 31.9 \pm 0.3$  km and  $\kappa = 1.7 \pm 0.01$ . We perform the anisotropic stacking procedure using the isotropic result as a constraint with an interval for  $H$  of  $30 \pm 5$  km and with  $\kappa$  of  $1.75 \pm 0.15$ . The result of the anisotropic analysis leads to  $H = 30.6 \pm 0.3$  km,  $\kappa = 1.76 \pm 0.01$ ,  $a = 3.7 \pm 0.6$  per cent (corresponding to a splitting time of  $0.32 \pm 0.05$  s) and  $\phi = 147 \pm 5^\circ$  with a robust and stable solution in the bootstrapping. The results are in good agreement with those of Kaviani & Rumpker (2015), who find a (slightly larger) splitting time of  $0.41 \pm 0.17$  s, a fast axis direction of  $-43$  ( $137^\circ$ )  $\pm 17^\circ$ , a thickness of  $31.5 \pm 1.1$  km and a velocity ratio of  $1.70 \pm 0.05$ . The comparison of the isotropic and anisotropic solutions shows that the inclusion of anisotropy leads to an improvement (amplitude increase) of the stacked waveform, whereas the isotropic procedure results in an amplitude only slightly larger than that obtained from a plain stack of the receiver-function waveforms (not performing any preceding moveout correction before the stack). This supports the conclusion of Kaviani & Rumpker (2015) who prefer the results of the anisotropic stacking despite the small change for depth and velocity ratio compared to the isotropic analysis.

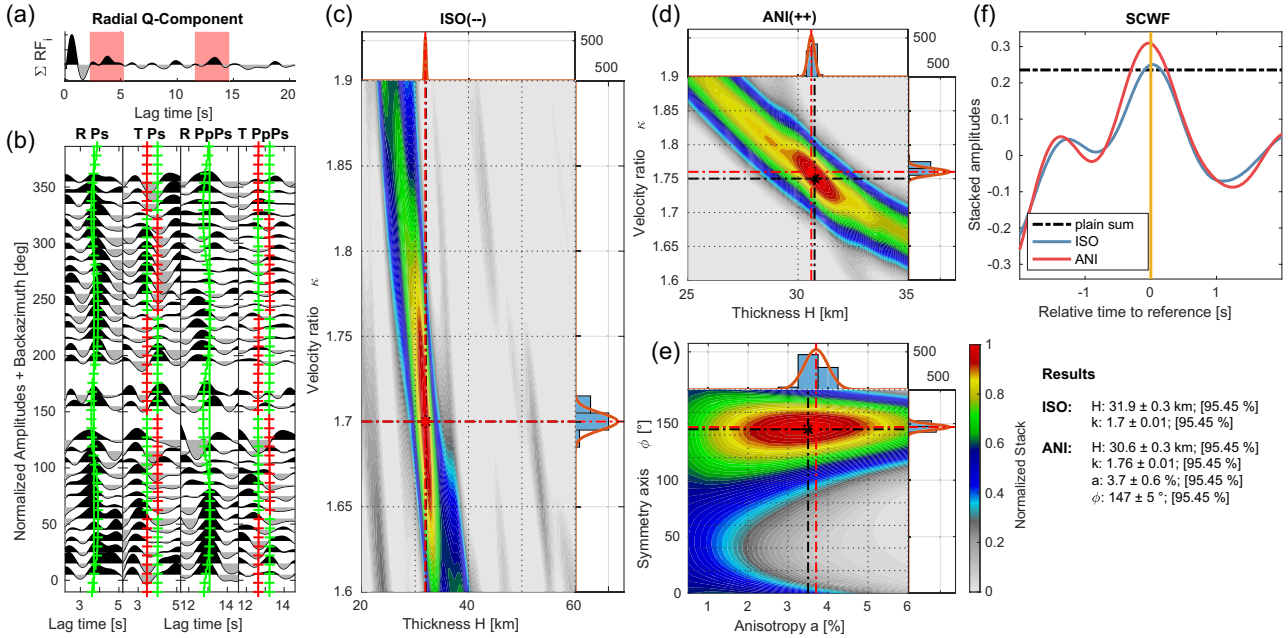


**Figure 10.** Same as Fig. 7, but for data of station GRFO of network IU. The anisotropic analysis (d–e) yields a stable solution with clear improvement in the coherency of the stacked waveforms (f).

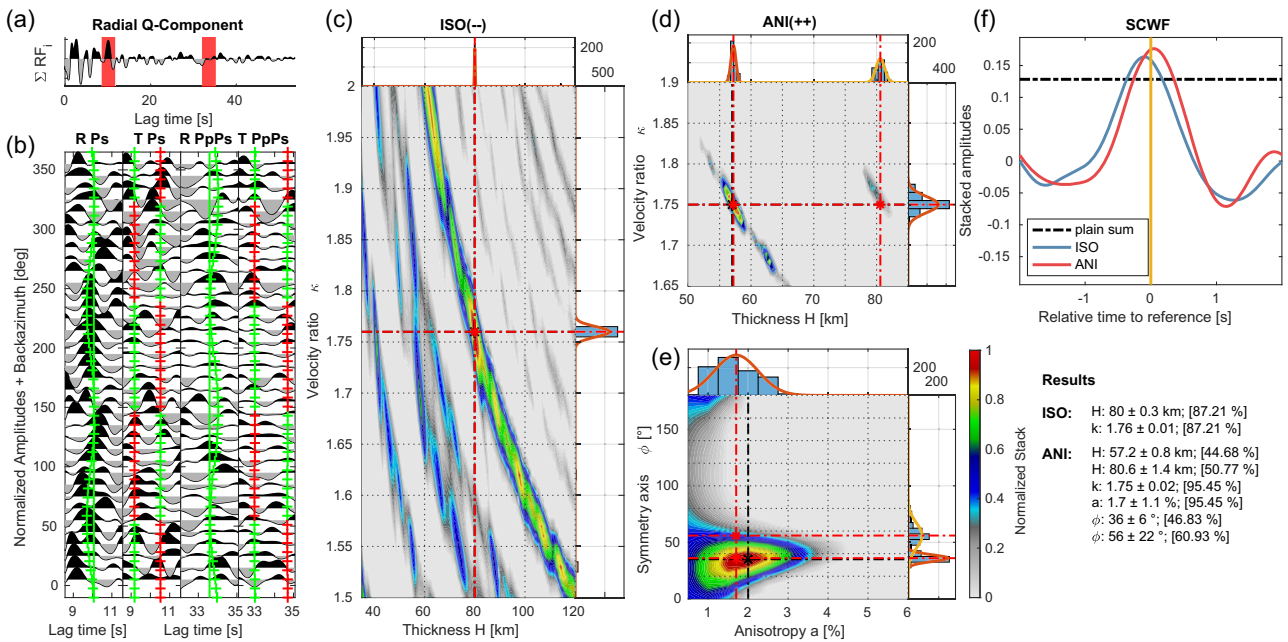


**Figure 11.** Same as Fig. 7, but for data of station LSA of the network IC. In the distribution of layer thickness and symmetry axis direction of the anisotropic analysis (ANI, e) there appear two separated groups, which are fitted separately by a Gaussian function. The probability is normalized on the total number of realizations used in the bootstrapping. This results in two solutions of almost equal probability. The anisotropy corresponds to splitting times of  $0.27 \pm 0.19$  s for the solution at  $\sim 57$  km and  $0.38 \pm 0.26$  s for the solution at  $\sim 80$  km.

In our next example, we analyse receiver functions for station LSA (see Fig. 11). We observe strong positive phases at  $\sim 7$  and  $\sim 10$  s, which possibly originate from the Moho interface. Previous studies suggest a doublet Moho with interfaces at 60 and 80 km (Priestley *et al.* 2008; Li *et al.* 2011). We first apply the isotropic  $H$ - $\kappa$ -stacking to identify the phase that produces the strongest maximum in the stacking of the radial receiver functions. We allow for variations in the Moho depth between 40 and 120 km. The result clearly points to a maximum at  $80 \pm 0.3$  km with a velocity ratio of  $1.76 \pm 0.01$ . The main maximum and subsequent side maxima show a clear dominance of the Ps-phase at  $\sim 10$  s, while energy also adds up coherently for a solution at depths of about 57 to 61 km. Therefore, we apply the anisotropic stacking procedure for a broad depth range between 40 and 85 km. Here the full stacking function provides a clear preference of the Ps-phase at  $\sim 7$  s resulting in a

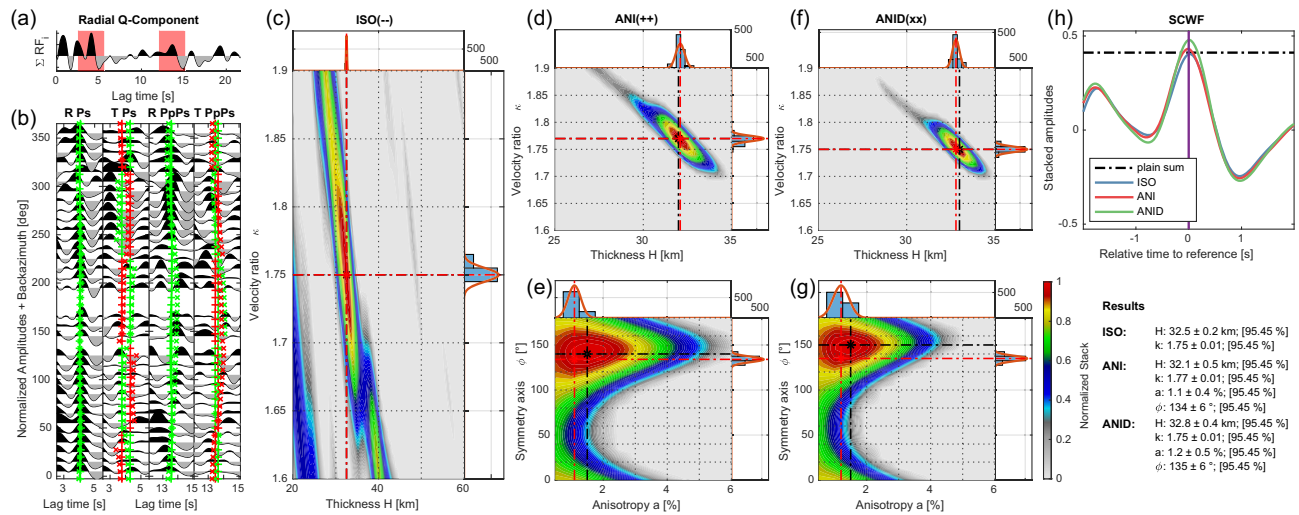


**Figure 12.** Same as Fig. 7, but for data of station TORNY of the network CH. (f–g) Stacking functions for anisotropic analysis with layer dip (ANID) of  $5.9^\circ$ . The inclusion of the layer dip produces a stable solution with slightly higher coherency of the stacked waveforms (f). The anisotropy corresponds to a splitting time of  $0.13 \pm 0.04$  s for ANI and  $0.14 \pm 0.06$  s for ANID.

maximum at  $57.2 \pm 0.8$  km. The maximum at  $\sim 80$  km is strongly suppressed. However, the bootstrapping shows, that this dominance is quite unstable with an equally probable solution at 80 km. The probability for the two individual groups is derived using

$$P_i = 0.9545 \frac{N_i}{N_{\text{tot}}}, \quad (16)$$

where  $P_i$  is the probability of the fitted group,  $N_i$  is the number of results in the group and  $N_{\text{tot}}$  is the total number of iterations (800) used in the bootstrapping. This example emphasizes the significance of a statistical recombination of subsets of the receiver functions to avoid an overweighting of traces. The strength of anisotropy remains the same for both solutions, whereas the fast-axis direction shifts slightly. The similarities suggest that the main source of anisotropy is found above 57 km, with a small portion of anisotropy present between 57 and 80 km. For both phases we observe strong energy on the transverse component and relatively weak coherency of the moveout corrected waveforms. This indicates the presence of structural complexity, which may need further investigation. However, this is beyond the scope of this study.

As the last example we have chosen station TORNY. Several studies have shown that the crust in this region is thickened due to the alpine collision accompanied by a dip of the Moho. The model of Waldhauser *et al.* (1998) provides a high-resolution map of Moho depths compiled from active source experiments across the Western and Central Alps. Based on the results of this study, we derive a dip of  $5.6^\circ$  and a strike of  $69.8^\circ$  for the Moho at the location of TORNY. These values are kept fixed in the anisotropic stacking. The receiver functions show three subsequent strong phases within the first 5 s indicating a thick sedimentary layer and a mid-crustal discontinuity. The Ps and PpPs phases from the Moho are clearly visible and lead to a stable and unique solution in the isotropic stacking with a thickness of  $H = 32.4 \pm 0.2$  km and  $\kappa = 1.75 \pm 0.01$  (see Fig. 12). This result coincides well with the Moho depth provided by previous studies (Waldhauser *et al.* 1998; Lombardi *et al.* 2008). The anisotropic analysis without (ANI) and with layer dip (ANID) leads to very similar solutions for all parameters. However, the stack of the moveout corrected waveforms shows a clear preference for the model with layer dip. This emphasizes the importance of including available structural information in the analysis and shows the necessity of reliable information to quantify a dip of the Moho.

## DISCUSSION AND CONCLUSION

The main aim of this paper is to provide a robust tool to derive the elastic parameters of the crust from receiver functions. Besides the thickness of the crust and the ratio of seismic velocities  $\frac{v_p}{v_s}$ , we include anisotropic parameters in the analysis. The procedure represents a modification of the anisotropic  $H$ - $\kappa$ -stacking of Kaviani & Rüpker (2015) by deriving all parameters simultaneously and also by allowing for a dipping layer boundary. For this purpose, we combine a classical splitting analysis of the Ps- and PpPs-phases with the stacking of the amplitudes after correction for the splitting effect. We first compute theoretical arrival times and polarization angles for the fast and slow phases in a given anisotropic model. Then, the amplitudes in receiver functions are picked according to the computed arrival times and rotated into the fast and slow coordinate system using the polarization angles. The fast and slow amplitudes are time-shifted to correct for the splitting delay time. After rotating back into the radial/transverse coordinate system the stacking is performed and the maximum of the stacking function yields the anisotropic parameters of the crust. This procedure can be seen as a simultaneous splitting analysis for two phases (Ps and PpPs). While Kaviani & Rüpker (2015) also consider further multiples in their analysis for the structural crustal parameters to stabilize the results, this would lead to unwanted complexities in our approach, as a separation of fast and slow energy would not be possible for phases with

more than one *S*-wave leg under general conditions. In this case more than two fast and two slow phases would arrive at almost the same time at the receiver. However, here we have shown that we are still able to obtain stable results by focusing on the Ps- and PpPs-phases while also benefitting from the reduced computational time. A dip of the Moho can strongly bias the search for the anisotropic parameters. It can also have a significant effect on the ray path, changing the (apparent) backazimuth and the polarization of the incoming wave. The algorithm allows to fix the layer dip beneath a station before deriving the elastic parameters. While this study relies on previous results for a specific region to implement the layer dip, an extension of our approach to include a search for the strike and dip is currently under development.

We tested the applicability of the stacking approach using synthetic models and introduced bootstrapping statistics as a tool to reveal alternative solutions hidden in subsets of the stacking functions. As a result of the statistical analysis we obtain the most probable solutions (including probability and error estimates) by fitting of a normal distribution curve to (groups of) the results. We discriminate between different model classes (isotropic crust, anisotropic crust with a fast or slow symmetry axis, and anisotropic crust with layer dip), by performing an additional summation of the phases after moveout correction. The degree of coherence achieved for the different types of models allows to identify the most likely class that represents the crust. If the results for model classes differ, the coherency stack also shows distinct differences and can help to identify the model. If the coherency is not improved with growing complexity despite differing results, it is an indication of either a large noise contribution, which corrupts the data, and/or lateral/vertical heterogeneities, which cannot be explained by the simplified isotropic and anisotropic model assumptions. As the amplitude of the stacked waveforms after moveout correction largely depends on the quality of data, the strength of anisotropy, the event distribution and possible complexities in the actual crustal structure (e.g. velocity gradient instead of discontinuity), a definition of quantitative limits for the coherency is hardly possible. Therefore, this parameter must be understood as a qualitative measure, which allows to identify general improvements of data fit. The tests show that it is possible to distinguish between isotropic and anisotropic models even under realistic noise conditions and event distribution. A test with limited azimuthal event distribution implies that an application to temporary stations is in principle possible. However, this can still lead to ambiguous conclusions in case of additional complexities (e.g. lateral variation), due to the incomplete azimuthal information. It should be noted that discrimination between models with a fast or slow symmetry axis is not possible and that the resulting crustal parameters (layer thickness and velocity ratio) can be fundamentally different from real values. Anisotropic parameters (amount of the anisotropy and the directions of the fastest and slowest velocities) are less affected (taking the expected 90° shift for the fast direction into account). When interested in the anisotropic effect of the crust on complementary observations of anisotropy, for example XKS-splitting, the nature of symmetry is of no relevance and it is more convenient to restrict the analysis to fast-axis symmetry. However, knowledge of the petrophysical situation in a study area can help to narrow down the expected  $\frac{v_p}{v_s}$  ratio and therefore provide the necessary information about the nature of symmetry (see also Hammond 2014). The synthetic models are based on approximating the crust as one layer with bulk anisotropic properties, while the anisotropy is decoupled at the crust–mantle boundary. We show that this approximation is also valid for a strong anisotropic thin layer within an isotropic crust despite additional complexities in the receiver functions. We further show that a plunge of the symmetry axis has less influence on the results using the anisotropic stacking approach, when assuming a distinction between conversion depth (Moho) and the lower boundary of the anisotropic layer. The sole effect is a decrease of splitting time with growing plunge. We therefore suggest that the strength of anisotropy derived from our method corresponds to a minimum estimate for the bulk anisotropy present in the crust. We still admit that this is a simplification and that the conversion depth may indeed coincide with the anisotropic layer boundary. Indicators for the presence of a plunging symmetry axis in such a case have been described before (see Schulte-Pelkum & Mahan 2014; Eckhard & Rabbel 2011). While most of our models show a relatively small effect of the anisotropic layer to the results of the isotropic analysis, applying an anisotropic analysis provides several advantages. The shear-wave splitting effect results in a separation of the crustal phases depending on azimuth, which intensifies for the multiple phases (see Fig. 2). This produces ambiguities in the isotropic inversion, whereas they are resolved with the anisotropic stacking analysis (see also Kaviani & Rumpker 2015). Additionally, the information of the elastic properties within the crust is more complete by considering anisotropy, which allows for a better tectonic interpretation (e.g. stress directions, fossil anisotropy/tectonic history). Therefore, we suggest to generally apply the anisotropic analysis, if possible, as it complements the knowledge about the physical properties of the crust.

The real data examples confirm the applicability of the method and the advantage of the statistical bootstrapping analysis. The simultaneous inversion for structural and anisotropic parameters for the crust leads to similar results when compared to previous studies, while the additional statistical analysis proves to be a powerful tool in revealing non-unique solutions and their corresponding probabilities. The implementation of a Moho dip in the analysis of the crustal parameters allows to extend the stacking of receiver functions to a broader variety of tectonic settings. The comparison of the coherency using the moveout correction from the results of different model classes indicates a better fit to the data for a model with anisotropic crust. Therefore, we suggest to generally include the anisotropic stacking in the standard analysis procedure. This is further encouraged when a large amount of transverse energy is associated with arrivals of the crustal phases. The method allows to evaluate whether this energy can be (partially) explained by anisotropy. It also provides estimates for possible differences in the results using isotropic or anisotropic model assumptions. Our examples indicate that the crust exhibits a considerable amount of anisotropy which can influence the results from deeper probing methods such as XKS-splitting. The new approach can be used to isolate the anisotropic effect of the crust and thus improves the analysis of mantle anisotropy (see Latifi *et al.* 2018). It complements the suite of methods available for probing deeper (mantle) anisotropy, especially in view of the inherent lack of depth resolution of conventional shear-wave splitting analyses. For example, the results can be used to constrain the splitting parameters of the upper layer in applications of a two-layer splitting analysis to better isolate mantle anisotropy. The remaining split of the waveforms can then be further investigated, to resolve layered anisotropy in

the mantle, if azimuthal variation remain to be significant (see Latifi *et al.* 2018). Therefore, the method can help to better constrain the anisotropic source region and improves the understanding of tectonic processes.

## ACKNOWLEDGEMENTS

We thank the IRIS Data Services, and specifically the IRIS Data Management Center for providing the waveform data and related metadata from stations GRFO (part of the Global Seismograph Network IU, <https://doi.org/10.7914/SN/IU>), LSA (part of the New China Digital Seismograph Network IC, <https://doi.org/10.7914/SN/IC>) and TORNY (part of the National Seismic Networks of Switzerland CH, <https://doi.org/10.12686/sed/networks/ch>) presented in this paper. IRIS Data Services are funded through the Seismological Facilities for the Advancement of Geoscience (SAGE) Award of the National Science Foundation under Cooperative Support Agreement EAR-1851048. We would also like to thank James Hammond and an anonymous reviewer for their constructive and very helpful comments. We acknowledge support from the German Research Foundation (DFG) through research grants to AK and GR.

## REFERENCES

- Ando, M., Ishikawa, Y. & Wada, H., 1980. S-wave anisotropy in the upper mantle under a volcanic area in Japan, *Nature*, **286**, 43–46.
- Babuska, V. & Cara, M., 1991. *Seismic Anisotropy in the Earth*, Vol. 10 of Modern Approaches in Geophysics, Springer.
- Backus, G.E., 1962. Long-wave elastic anisotropy produced by horizontal layering, *J. geophys. Res.*, **67**, 4427–4440.
- Barruol, G. & Mainprice, D., 1993. A quantitative evaluation of the contribution of crustal rocks to the shear-wave splitting of teleseismic SKS waves, *Phys. Earth planet. Inter.*, **78**(3–4), 281–300.
- Bianchi, I., Bokelmann, G. & Shiomi, K., 2015. Crustal anisotropy across northern Japan from receiver functions, *J. geophys. Res.*, **120**(7), 4998–5012.
- Bianchi, I. & Bokelmann, G.H.R., 2014. Seismic signature of the Alpine indentation, evidence from the Eastern Alps, *J. Geodyn.*, **82**, 69–77.
- Bianchi, I., Park, J., Agostinetti, N.P. & Levin, V., 2010. Mapping seismic anisotropy using harmonic decomposition of receiver functions: an application to Northern Apennines, Italy, *J. geophys. Res.*, **115**(B12), doi:10.1029/2009JB007061.
- Blackman, D.K. & Kendall, J.-M., 1997. Sensitivity of teleseismic body waves to mineral texture and melt in the mantle beneath a mid-ocean ridge, *Phil. Trans. R. Soc. Lond., A*, **355**(1723), 217–231.
- Bowman, J.R. & Ando, M., 1987. Shear-wave splitting in the upper-mantle wedge above the Tonga subduction zone, *Geophys. J.*, **88**, 25–41.
- Cheng, B., Zhao, D., Cheng, S., Ding, Z. & Zhang, G., 2016. Seismic tomography and anisotropy of the Helan-Liupan tectonic belt: Insight into lower crustal flow and seismotectonics, *J. geophys. Res.*, **121**(4), 2608–2635.
- Christensen, N.I., 1966. Shear wave velocities in metamorphic rocks at pressures to 10 kilobars, *J. geophys. Res.*, **71**, 3549–3556.
- Cossette, É., Audet, P., Schneider, D. & Grasemann, B., 2016. Structure and anisotropy of the crust in the Cyclades, Greece, using receiver functions constrained by in situ rock textural data, *J. geophys. Res.*, **121**(4), 2661–2678.
- Crampin, S., 1987. The basis for earthquake prediction, *Geophys. J.*, **91**, 331–347.
- Eaton, D.W., Dineva, S. & Mereu, R., 2006. Crustal thickness and Vp/Vs variations in the Grenville orogen (Ontario, Canada) from analysis of teleseismic receiver functions, *Tectonophysics*, **420**(1–2), 223–238.
- Eckhardt, C. & Rabbel, W., 2011. P-receiver functions of anisotropic continental crust: a hierarchic catalogue of crustal models and azimuthal waveform patterns, *Geophys. J. Int.*, **187**(1), 439–479.
- Efron, B., 1979. Bootstrap methods: another look at the jackknife, *Ann. Stat.*, **7**(1), 1–26.
- Farra, V., Vinnik, L.P., Romanowicz, B., Kosarev, G.L. & Kind, R., 1991. Inversion of teleseismic S particle motion for azimuthal anisotropy in the upper mantle: a feasibility study, *Geophys. J. Int.*, **106**(2), 421–431.
- Frederiksen, A.W. & Bostock, M.G., 2000. Modelling teleseismic waves in dipping anisotropic structures, *Geophys. J. Int.*, **141**(2), 401–412.
- Fry, B., Deschamps, F., Kissling, E., Stehly, L. & Giardini, D., 2010. Layered azimuthal anisotropy of Rayleigh wave phase velocities in the European Alpine lithosphere inferred from ambient noise, *Earth planet. Sci. Lett.*, **297**(1–2), 95–102.
- Fryer, G.J. & Frazer, L.N., 1984. Seismic waves in stratified anisotropic media, *Geophys. J. Int.*, **78**(3), 691–710.
- Guest, W.S., Thomson, C.J. & Spencer, C.P., 1993. Anisotropic reflection and transmission calculations with application to a crustal seismic survey from the East Greenland Shelf, *J. geophys. Res.*, **98**(B8), 14161–14184.
- Hammond, J.O.S., 2014. Constraining melt geometries beneath the Afar Depression, Ethiopia from teleseismic receiver functions: the anisotropic H- $\kappa$  stacking technique, *Geochem. Geophys. Geosyst.*, **15**(4), 1316–1332.
- Hua, Y., Zhao, D. & Xu, Y., 2017. P wave anisotropic tomography of the Alps, *J. geophys. Res.*, **122**, 4509–4528.
- Ji, S., Salisbury, M.H. & Hammer, S., 1993. Petrofabric, P-wave anisotropy and seismic reflectivity of high-grade tectonites, *Tectonophysics*, **222**(2), 195–226.
- Kaviani, A. & Rumpker, G., 2015. Generalization of the H- $\kappa$  stacking method to anisotropic media, *J. geophys. Res.*, **120**(7), 5135–5153.
- Kind, R., Kosarev, G.L. & Petersen, N.V., 1995. Receiver functions at the stations of the German Regional Seismic Network (GRSN), *Geophys. J. Int.*, **121**(1), 191–202.
- Krüger, F. & Weber, M., 1992. The effect of low-velocity sediments on the mislocation vectors of the GRF array, *Geophys. J. Int.*, **108**(1), 387–393.
- Langston, C.A., 1979. Structure under Mount Rainier, Washington, inferred from teleseismic body waves, *J. geophys. Res.*, **84**(B9), 4749–4762.
- Latifi, K., Kaviani, A., Rumpker, G., Mahmoodabadi, M., Ghassemi, M.R. & Sadidkhouy, A., 2018. The effect of crustal anisotropy on SKS splitting analysis—synthetic models and real-data observations, *Geophys. J. Int.*, **213**(2), 1426–1447.
- Levin, V. & Park, J., 1997. P-SH conversions in a flat-layered medium with anisotropy of arbitrary orientation, *Geophys. J. Int.*, **131**(2), 253–266.
- Liu, H. & Niu, F., 2012. Estimating crustal seismic anisotropy with a joint analysis of radial and transverse receiver function data, *Geophys. J. Int.*, **188**(1), 144–164.
- Liu, Z. & Park, J., 2017. Seismic receiver function interpretation: P s splitting or anisotropic underplating?, *Geophys. J. Int.*, **208**(3), 1332–1341.
- Li, X., Wei, D., Yuan, X., Kind, R., Kumar, P. & Zhou, H., 2011. Details of the doublet Moho structure beneath Lhasa, Tibet, obtained by comparison of P and S receiver functions, *Bull. seism. Soc. Am.*, **101**(3), 1259–1269.
- Lombardi, D., Braunmiller, J., Kissling, E. & Giardini, D., 2008. Moho depth and Poisson's ratio in the Western-Central Alps from receiver functions, *Geophys. J. Int.*, **173**(1), 249–264.
- Love, A.E.H., 1926. *A Treatise on the Mathematical Theory of Elasticity*, University Press.
- Mainprice, D., 1997. Modelling the anisotropic seismic properties of partially molten rocks found at mid-ocean ridges, *Tectonophysics*, **279**(1–4), 161–179.
- McNamara, D.E. & Owens, T.J., 1993. Azimuthal shear wave velocity anisotropy in the Basin and Range Province using Moho Ps converted phases, *J. geophys. Res.*, **98**(B7), 12003–12017.
- Nagaya, M., Oda, H., Akazawa, H. & Ishise, M., 2008. Receiver functions of seismic waves in layered anisotropic media: application to the estimate of seismic anisotropy, *Bull. seism. Soc. Am.*, **98**(6), 2990–3006.
- Nur, A., 1971. Effects of stress on velocity anisotropy in rocks with cracks, *J. geophys. Res.*, **76**(8), 2022–2034.

- Nur, A. & Simmons, G., 1969. Stress-induced velocity anisotropy in rock: An experimental study, *J. geophys. Res.*, **74**(27), 6667–6674.
- Okaya, D.A. & McEvilly, T.V., 2003. Elastic wave propagation in anisotropic crustal material possessing arbitrary internal tilt, *Geophys. J. Int.*, **153**(2), 344–358.
- Priestley, K., Jackson, J. & McKenzie, D., 2008. Lithospheric structure and deep earthquakes beneath India, the Himalaya and southern Tibet, *Geophys. J. Int.*, **172**(1), 345–362.
- Reiss, M.C. & Rumpker, G., 2017. SplitRacer: MATLAB code and GUI for semiautomated analysis and interpretation of teleseismic shear-wave splitting, *Seismol. Res. Lett.*, **88**(2A), 392–409.
- Reiss, M.C., Rumpker, G. & Wölbern, I., 2018. Large-scale trench-normal mantle flow beneath central South America, *Earth planet. Sci. Lett.*, **482**, 115–125.
- Rumpker, G., Kaviani, A. & Latifi, K., 2014. Ps-splitting analysis for multilayered anisotropic media by azimuthal stacking and layer stripping, *Geophys. J. Int.*, **199**(1), 146–163.
- Sambridge, M., 1999. Geophysical inversion with a neighbourhood algorithm—II. Appraising the ensemble, *Geophys. J. Int.*, **138**(3), 727–746.
- Savage, M.K., 1998. Lower crustal anisotropy or dipping boundaries? Effects on receiver functions and a case study in New Zealand, *J. geophys. Res.*, **103**(B7), 15069–15087.
- Savage, M.K., 1999. Seismic anisotropy and mantle deformation: what have we learned from shear wave splitting?, *Rev. Geophys.*, **37**, 65–106.
- Savage, M.K., Wessel, A., Teanby, N.A. & Hurst, A.W., 2010. Automatic measurement of shear wave splitting and applications to time varying anisotropy at Mount Ruapehu volcano, New Zealand, *J. geophys. Res.*, **115**(B12), doi:10.1029/2010JB007722.
- Savage, M.K. *et al.*, 2016. Stress, strain rate and anisotropy in Kyushu, Japan, *Earth planet. Sci. Lett.*, **439**, 129–142.
- Schulte-Pelkum, V. & Mahan, K.H., 2014. A method for mapping crustal deformation and anisotropy with receiver functions and first results from USArray, *Earth planet. Sci. Lett.*, **402**, 221–233.
- Shih, X.R., Meyer, R.P. & Schneider, J.F., 1989. An automated, analytical method to determine shear-wave splitting, *Tectonophysics*, **165**(1–4), 271–278.
- Silver, P.G. & Chan, W.W., 1988. Implications for continental structure and evolution from seismic anisotropy, *Nature*, **335**, 34–39.
- Silver, P.G. & Chan, W.W., 1991. Shear wave splitting and subcontinental mantle deformation, *J. geophys. Res.*, **96**(B10), 16429–16454.
- Sun, Y., Liu, J., Zhou, K., Chen, B. & Guo, R., 2015. Crustal structure and deformation under the Longmenshan and its surroundings revealed by receiver function data, *Phys. Earth planet. Inter.*, **244**, 11–22.
- Waldhauser, F., Kissling, E., Ansgor, J. & Mueller, S., 1998. Three-dimensional interface modelling with two-dimensional seismic data: the Alpine crust-mantle boundary, *Geophys. J. Int.*, **135**(1), 264–278.
- Wang, J. & Zhao, D., 2008. P-wave anisotropic tomography beneath Northeast Japan, *Phys. Earth planet. Inter.*, **170**(1–2), 115–133.
- Wang, J. & Zhao, D., 2013. P-wave tomography for 3-D radial and azimuthal anisotropy of Tohoku and Kyushu subduction zones, *Geophys. J. Int.*, **193**(3), 1166–1181.
- Wang, P., Huang, Z. & Wang, X., 2020. A method for estimating the crustal azimuthal anisotropy and Moho orientation simultaneously using receiver functions, *J. geophys. Res.*, **125**(2), e2019JB018405.
- Wang, Q., Niu, F., Gao, Y. & Chen, Y., 2016. Crustal structure and deformation beneath the NE margin of the Tibetan plateau constrained by teleseismic receiver function data, *Geophys. J. Int.*, **204**(1), 167–179.
- Wirth, E.A. & Long, M.D., 2014. A contrast in anisotropy across mid-lithospheric discontinuities beneath the central United States—A relic of craton formation, *Geology*, **42**(10), 851–854.
- Woodhouse, J.H., 1974. Surface waves in a laterally varying layered structure, *Geophys. J. Int.*, **37**(3), 461–490.
- Wölbern, I. & Rumpker, G., 2017. Limitations of H- $\kappa$  stacking: ambiguous results caused by crustal layering, *J. Seismol.*, **21**, 221–235.
- Wüstefeld, A., Bokelmann, G., Zaroli, C. & Barruol, G., 2008. SplitLab: A shear-wave splitting environment in Matlab, *Comput. Geosci.*, **34**(5), 515–528.
- Yousef, B.M. & Angus, D.A., 2016. When do fractured media become seismically anisotropic? Some implications on quantifying fracture properties, *Earth planet. Sci. Lett.*, **444**, 150–159.
- Zhao, D., Hasegawa, A. & Horiuchi, S., 1992. Tomographic imaging of P and S wave velocity structure beneath northeastern Japan, *J. geophys. Res.*, **97**(B13), 19909–19928.
- Zhao, D., Yu, S. & Liu, X., 2016. Seismic anisotropy tomography: new insight into subduction dynamics, *Gondwana Res.*, **33**, 24–43.
- Zhu, L. & Kanamori, H., 2000. Moho depth variation in southern California from teleseismic receiver functions, *J. geophys. Res.*, **105**(B2), 2969–2980.

## SUPPORTING INFORMATION

Supplementary data are available at *GJI* online.

**Figure S1.** Stacking analysis for synthetic data of model II. (a) Sum trace over all radial receiver functions. (b) Azimuthal stacks of the radial and transverse receiver functions are shown windowed around the Ps- and PpPs-phase (marked red in a). The following columns show the stacking function for the isotropic (ISO, c), anisotropic analyses assuming a fast axis (ANI, d–e) and an anisotropic analysis assuming a slow axis (ANI-S, f–g), respectively. The corresponding results are marked by the crossed lines and the corresponding lag times are marked in the azimuthally sorted receiver functions as solid line (indicated in the title as ‘—’) for the isotropic and marked by pluses (indicated in the title as ‘++’) for the anisotropic solution with fast axis and marked by crosses for the anisotropic solution with slow axis (indicated in the title as ‘xx’). Red and green colors indicate the expected sign of the amplitude for this arrival. (h) Moveout corrected stack of waveforms (SCWF) for the two solutions in comparison to a plain stack of the receiver functions (black dashed line). The maximum with the highest magnitude corresponds to the most coherent stack of the Ps- and PpPs-phase. The results of the analyses are given below on the right (indicated by ISO, ANI and ANID).

**Figure S2.** Same as Figure S1, but for model III. Here only the isotropic and anisotropic analyses, assuming a fast symmetry axis, is applied.

**Figure S3.** Example of producing a realistic receiver function by introducing a more complex signal and contaminated by noise. Top row: calculated traces for an anisotropic model with vertical, radial and transverse components. Middle row: calculated traces convolved with a more complex signal and contaminated with real pre-vent noise recorded at the station TNS. Bottom row: receiver function from deconvolution of the noisy traces. The original traces (shown as red dashed lines) are recovered well on the radial component, while the transverse component is contaminated with by the high noise level.

**Figure S4.** Same as Fig. S1, but for noise contaminated traces of model II and also simulating a random event distribution. The bar plots attached to the axes of the stacking functions present the results from the bootstrapping. The solid line is a fit of a Gaussian function to the

distribution normalized by the number of fitted elements. The mean and the  $2\sigma$ -interval from the standard deviation leads to the results in the right column. The  $2\sigma$ -interval corresponds to the probability of 95.45 per cent of all measurements of the fitted group to be located inside.

**Figure S5.** Same as figure S4, but for noise contaminated traces of model IV.

**Figure S6.** Same as figure S4, but for real data of station LSA. We show here an isotropic and anisotropic analysis focused on the Ps-phase at  $\sim 7$  s different from the analysis in the paper, where the analysis over a broad range of values for the layer-thickness allows a consistent discussion regarding the ambiguous solutions in the statistics.

Please note: Oxford University Press is not responsible for the content or functionality of any supporting materials supplied by the authors. Any queries (other than missing material) should be directed to the corresponding author for the paper.